# Probabilistic precipitation downscaling for ungauged mountain sites: a pilot study for the Hindu Kush Karakoram Himalaya

Marc Girona-Mata[1,2], Andrew Orr[2], Martin Widmann[3], Daniel Bannister[4], Ghulam Hussain Dars[5], Scott Hosking[2,6], Jesse Norris[7], David Ocio[8], Tony Phillips[2], Jakob Steiner[9,10], and Richard E. Turner[1]

[1]Department of Engineering, University of Cambridge, Cambridge, UK
[2]British Antarctic Survey, UK Research and Innovation, Cambridge, UK
[3]School of Geography, Earth and Environmental Sciences, University of Birmingham, Birmingham, UK
[4]WTW Research Network, WTW, London, UK
[5]U.S.-Pakistan Center for Advanced Studies in Water, Mehran University of Engineering and Technology, Jamshoro, Pakistan
[6]The Alan Turing Institute, London, UK
[7]Atmospheric and Oceanic Sciences, University of California Los Angeles, Los Angeles, CA, USA
[8]Mott MacDonald, Cambridge, UK
[9]Institute of Geography and Regional Science, University of Graz, Graz, Austria
[10]Himalayan University Consortium, Lalitpur, Nepal

**Correspondence:** Marc Girona-Mata (mg963@cam.ac.uk)

**Abstract.** This study introduces a novel approach to post-processing (i.e., downscaling and bias-correcting) reanalysis-driven regional climate model daily precipitation that is capable of generalising to ungauged mountain locations by leveraging sparse in situ observations and a probabilistic regression framework. We call this post-processing approach Generalised Probabilistic Regression (GPR), and implement it using both generalised linear models and artificial neural networks (i.e., multilayer perceptrons). By testing the GPR post-processing approach across three Hindu Kush-Karakoram-Himalaya basins with varying hydro-meteorological characteristics and four experiments, which are representative of real-world scenarios, we find it performs consistently much better than both raw regional climate model output and deterministic bias correction methods for generalising daily precipitation post-processing to ungauged locations. We also find that GPR models are flexible and can be trained using data from a single region or multiple regions combined together, without major impacts on model performance. Additionally, we show that the GPR approach results in superior skill for post-processing entirely ungauged regions, by leveraging data from other regions, as well as ungauged high-elevation ranges. This suggests that GPR models have potential for extending post-processing of daily precipitation to ungauged areas of HKH. Whilst multilayer perceptrons yield marginally improved results overall, generalised linear models are a robust choice particularly for data-scarce scenarios, i.e., post-processing extreme precipitation events and generalising to completely ungauged regions.

## 1 Introduction

The mountain ranges of High Mountain Asia, often referred to as the Water Towers of Asia (Immerzeel et al., 2010), are the source of many major rivers in South Asia, supplying water resources to a rich diversity of terrestrial and marine ecosystems (Xu et al., 2019) and to approximately 2 billion people living in or directly downstream of them (Bolch et al., 2012; Mukherji

et al., 2019; Wester et al., 2019; Widmann et al., 2019). These resources are heavily reliant on precipitation caused primarily by

20 large-scale atmospheric circulations, such as the Indian summer monsoon and winter westerly disturbances, interacting with the steep orography that characterises the southern rim of High Mountain Asia, comprising the Hindu Kush Karakoram Himalaya (HKH) mountain ranges (Bookhagen and Burbank, 2010; Palazzi et al., 2013; Baudouin et al., 2020; Dimri et al., 2015). Yet, despite the large human populations depending on these resources for power, industry, tourism, farming, and domestic consumption, the contributions of rain and snow (and its ensuing melt) to these river systems are still poorly studied and little

25 understood. This precipitation knowledge gap in HKH severely affects our ability to quantify its present-day water resources and associated stream flows (Immerzeel et al., 2015; Arfan et al., 2019; Li et al., 2018; Salzmann et al., 2014). Consequently, it constitutes the largest source of uncertainty when it comes to making effective and robust water management decisions (e.g., water infrastructure construction, water demand management) and their critical role in regulating regional water supply, as well as planning for the hydrological impacts of climate change (Chinnasamy et al., 2015; Momblanch et al., 2019; Wester et al.,

30 2019; Nie et al., 2021; Orr et al., 2022).

Improving our understanding of precipitation in the HKH region is highly challenging (e.g., Wester et al., 2019; Sabin et al., 2020; Orr et al., 2022). In particular, the extreme orography that characterises this region results in large precipitation variations over small spatio-temporal scales, which are poorly understood due to the sparse and uneven rain and snow gauge network across the region (Archer and Fowler, 2004; Bannister et al., 2019; Immerzeel et al., 2015; Bookhagen and Burbank,

35 2010; Baudouin et al., 2020; Pritchard, 2021). For example, an area of around 566,000 km$^2$ above 4000 m elevation in HKH is currently represented by a single long-running gauge station in the Global Historical Climatology Network database (Pritchard, 2021). This poor understanding of precipitation extends to localised extremes that result from the triggering of convective events by small-scale topographic features (Orr et al., 2017; Bhardwaj et al., 2021; Ren et al., 2017; Dimri et al., 2017; Thayyen et al., 2013; Potter et al., 2018), which are often associated with rapid hydrological responses as well as hydro-meteorological

40 hazards such as floods and landslides (Qazi et al., 2019; Lutz et al., 2016; Ji et al., 2020; Dimri et al., 2017; Thayyen et al., 2013; Das et al., 2006).

One of the approaches to overcome the issues related to the limited gauge networks in HKH has been to develop daily gridded datasets with wide spatial and temporal coverage. These include gauge-based products such as the Asian Precipitation Highly Resolved Observational Data Towards Evaluation of Water Resources (APHRODITE; Yatagai et al., 2012), satellite-

45 based products such as the Tropical Rainfall Measuring Mission (TRMM; Huffman et al., 2007), climate reanalysis products such as ECMWF Reanalysis v5 (ERA5; Hersbach et al., 2020), and multi-source products such as the Multi-Source Weighted-Ensemble Precipitation (MSWEP; Beck et al., 2019), which merges gauge, satellite, and reanalysis data. However, in HKH these datasets are characterised by large differences in both climatological and extreme precipitation values, with the lack of consensus confirming that our understanding of precipitation characteristics in this region is extremely poor (Bannister et al.,

50 2019; Palazzi et al., 2013; Li et al., 2018). The large differences between these datasets are explained by the different types of observations used in them, as well as the methods used to compile them. For example, APHRODITE relies on distance-weighted interpolation of gauge values to derive precipitation patterns, which are difficult to robustly calculate in HKH due to the lack of in situ observations, as well as the large spatio-temporal precipitation gradients (Bannister et al., 2019; Ji et al.,

2020; Luo et al., 2020; Andermann et al., 2011). Recent alternatives such as MWSEP (Beck et al., 2019), which is arguably one of the best global precipitation datasets, also relies on gauge data and is therefore much less well constrained to observations in HKH compared to elsewhere. Consequently, alternative tools are needed to better understand the detailed spatio-temporal characteristics of precipitation in HKH.

Dynamical downscaling of coarse spatial resolution reanalysis datatsets (e.g., approximately 30 km for ERA5) using a regional climate model (RCM) is increasingly being used to produce high-resolution gridded precipitation products over HKH (Norris et al., 2020; Bannister et al., 2019; Maussion et al., 2011; Wang et al., 2021). These RCMs are characterised by spatial resolutions from 1-10 km that are generally able to resolve the complex terrain and thus better represent precipitation variability, and especially extremes. However, RCM outputs are still subject to errors and uncertainty (Giorgi, 2019), which can be exacerbated in mountain areas due to the complexity of the terrain (Sanjay et al., 2017; ul Hasson et al., 2019). For example, while reanalysis-driven RCM simulations are able to capture the large-scale circulation accurately (e.g., summer monsoon and westerly disturbances) by using either nudging or frequent initialisation techniques (Norris et al., 2020; Bannister et al., 2019; Maussion et al., 2011; Wang et al., 2021), they can still be subject to deficiencies in the representation of key physical processes such as the local valley wind regime, boundary layer, and cloud microphysics (Orr et al., 2017; Potter et al., 2018), as well as discrepancies between real and simulated orography (Eden et al., 2012). Statistical post-processing techniques, such as bias correction, are therefore often applied to improve the accuracy of RCM outputs, including precipitation (e.g., Shrestha et al., 2017; Bannister et al., 2019; Dimri, 2021; Tazi et al., 2023).

The model output statistics (MOS) approach to bias-correcting RCM simulations involves developing statistical relationships between RCM outputs, used as predictors, and observations, used as predictands (e.g., Klein and Glahn, 1974; Maraun and Widmann, 2018). MOS post-processing methods are usually deployed in either single-site or multi-site fashion to correct RCM simulations for locations where observations are available. However, in settings where gauge measurements are spatially sparse, MOS post-processing can also be used to adjust RCM precipitation output at ungauged locations (e.g., Samuel et al., 2012). In regions such as HKH where standard spatial interpolation techniques fail to capture the local-scale spatio-temporal precipitation variability, such an approach is fundamental; yet, it has not received much attention in the past. Bannister et al. (2019) applied bias correction to ungauged locations by using a deterministic, distribution-wise MOS method to adjust RCM precipitation outputs across two Himalayan basins. Additionally, MOS post-processing for bias correction can sometimes also involve downscaling RCM outputs to higher spatial resolutions (i.e. they correct for biases as well as downscale from a coarser to a finer scale). Hereafter, we use the term post-processing to refer to the combination of downscaling and bias-correcting.

Traditional MOS methods post-process the marginal distribution of the RCM output deterministically. In this setting, a specific set of predictors always yields the same corrected value and the spatio-temporal structure of the simulated output is not explicitly altered. This implicitly assumes that local-scale spatio-temporal variability is completely captured by the RCM-simulated gridbox variability. Whilst this assumption might hold in the case of pure bias correction, if the post-processing also involves downscaling to point observations (or higher-resolution gridded data) then deterministic approaches are not appropriate and a probabilistic method should be used instead (Maraun, 2013). Furthermore, using regression-based MOS

methods, the synchrony (or pair-wise correspondence) between reanalysis-driven RCMs and observations can be leveraged to correct for biases in the temporal representation of RCM precipitation outputs, which can often be large (Lafon et al., 2013).

Previous studies have developed regression-based MOS methods based on artificial neural networks to statistically post-process precipitation (e.g., Cannon, 2008; Sachindra et al., 2018; Baño-Medina et al., 2020; Vaughan et al., 2021). For example, the multi-site precipitation downscaling framework proposed by Cannon (2008) employs artificial neural networks for probabilistic regression. More advanced regression-based MOS model architectures have also been leveraged recently to undertake this task, including convolutional neural networks (Baño-Medina et al., 2020), autoencoders (Vandal et al., 2019), and neural processes (Vaughan et al., 2021). However, all these methods generally rely on the availability of abundant training data, and thus focus on data-rich regions. The potential of regression-based MOS post-processing for ungauged mountain locations (such as in HKH) remains untapped.

In this pilot study, we introduce the Generalised Probabilistic Regression (GPR) MOS approach for post-processing (i.e., downscaling and bias-correcting) RCM daily precipitation outputs using sparse gauge data in HKH. This approach extends the pairwise stochastic MOS framework proposed by Wong et al. (2014) and leverages probabilistic regression models (i.e., generalised linear models and multi-layer perceptrons). The key advantage of the GPR approach is that is it capable of generalising to ungauged locations, whilst also capturing the uncertainty that arises both from this spatio-temporal generalisation and from the asynchronous timing of precipitation between RCM output and observations. Thus, using the GPR approach we can leverage a discrete and relatively sparse network of in situ observations to improve precipitation maps (i.e., gridded products) for HKH whilst quantifying the uncertainty of our estimates. The GPR approach can also be viewed as a probabilistic spatio-temporal interpolation technique for daily precipitation observations informed by (or conditioned on) RCM simulations and other contextual factors. Furthermore, the framework we employ is, in essence, a conditional MOS precipitation generator that is consistent with the RCM-simulated weather (Cannon, 2008; Wong et al., 2014).

We test the GPR framework by post-processing daily precipitation output from an RCM simulation of HKH produced using the Weather Research and Forecasting (WRF) model for three target regions, namely, the eastern and western reaches of the Upper Indus Basin, and the central part of the Upper Ganges Basin, which hereafter are referred to as East UIB, West UIB, and Central UGB respectively (Fig. 1). Together, these three regions span a wide portion of HKH and have very different characteristics in terms of geography, orography, climatology and observational network / data availability, i.e., providing a diverse range of conditions / challenges for the GPR framework in order to robustly test it. Finally, although the focus of this study is HKH, the results of this exercise should be applicable to other data-sparse mountain ranges in the world.

## 2 Data and Methods

### 2.1 Target regions and datasets

The West UIB region includes the Gilgit-Baltistan area, which is located in Karakoram and western Himalaya (Fig. 1). The Gilgit-Baltistan area is 72,971 km$^2$ in size, and includes the Hunza and Gilgit rivers, as well as the main branch of the Indus (Iqbal et al., 2019). For this study, the daily precipitation records available for this area consist of 12 stations over the period
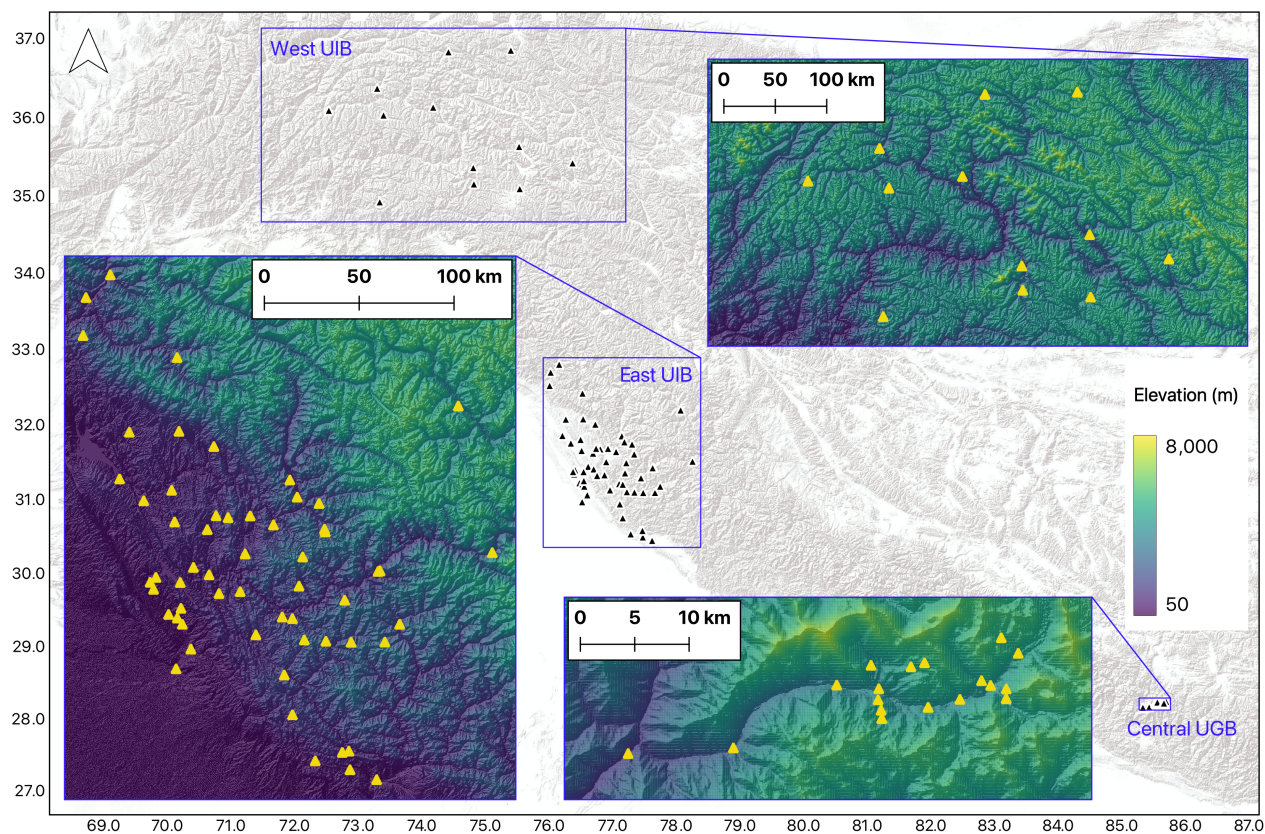
**Figure 1.** Map showing the three target regions across HKH: West Upper Indus Basin (West UIB), East Upper Indus Basin (East UIB), and Central Upper Ganges Basin (Central UGB), including the location of the gauge measurements (black triangles). Inset maps show more detail for each of the target regions, including the elevation of the topography (shading) and the location of gauge measurements (yellow triangles). The topography dataset shown in the inset maps is from the Shuttle Radar Topography Mission (SRTM) digital elevation model.

**Table 1.** Elevation range and summary of the stations used to provide daily precipitation observations for each of the three target regions. Note that each station contains gaps in the instrumental record.

| Region | Elevation range (m.a.s.l.) | No. stations | Period covered | No. datapoints |
|--------|---------------------------|--------------|----------------|----------------|
| West UIB | 1,460 - 4,707 | 12 | 1995-2014 | 76,860 |
| East UIB | 265 - 3,645 | 58 | 1980-2013 | 364,713 |
| Central UGB | 1,406 - 5,090 | 20 | 2012-2014 | 15,152 |

1995-2015 (comprising a total of 76,860 data points), which range from 1,460 to 4,707 meters above sea level (m.a.s.l.) (Table 1). The average distance between neighbouring stations is around 60 km.

The East UIB region includes the Sutlej River basin and the Beas River basin, which are situated in western Himalaya. The Sutlej River basin has an area of 60,803 km$^2$ (above the Bhakra dam) and its river is the largest and easternmost of the tributaries of the Indus (Fig. 1). The Beas River basin has an area of 12,286 km$^2$ (above the Pong dam) and its river is itself a tributary of the Sutlej River. The available daily precipitation records in these basins (and neighbouring areas) come from 58 stations over the period 1980-2013 (364,713 data points), which range from 256 to 3,645 m.a.s.l. (Table 1). The majority of the stations are located in the lower reaches of both catchments (Fig. 1), i.e., a significant part of the catchment area sits at elevations above the highest monitoring station. The average distance between neighbouring stations is around 15 km, which constitutes a relatively-dense network of precipitation measurements compared to West UIB, as well as many other areas in HKH (Nepal et al., 2023).

The Central UGB region includes the Langtang River catchment, which is situated in central Himalaya (Fig. 1). It consists of a relatively small area, and its river is a tributary to the Ganges (Fig. 1). The available daily precipitation records for this region come from 21 stations from 2012-2014 (15,152 data points), which range from 1,406 to 5,090 m.a.s.l. (Table 1). The average distance between neighbouring stations is less than 2 km, which makes this one of the most dense networks of precipitation measurements in HKH (Steiner et al., 2021; Shea et al., 2015).

The WRF simulation is by Norris et al. (2019). It dynamically downscales 36 years of Climate Forecast System Reanalyses data (Saha et al., 2010) from 1979 to 2015 over HKH at a spatial resolution of 6.7 km. We use multiple outputs (including daily precipitation) from this simulation from 1980 to 2014 that cover the three target regions (see Table 2). Norris et al. (2019) found that daily precipitation output from this simulation was better correlated with HKH gauge data in winter (correlation coefficient of 0.70) than in summer (correlation coefficient of 0.56). Additionally, over the Karakoram (West UIB), the simulated precipitation had a relatively substantial negative bias (Norris et al., 2017). Note that the station data described above and the WRF precipitation output are independent, i.e., the data was not assimilated into the Climate Forecast System Reanalysis. Finally, the terrain elevation of the three target regions (and stations) is taken from the Shuttle Radar Topography Mission (SRTM) digital elevation model, which has a spatial resolution of 30 m.

## 2.2 Generalised Probabilistic Regression (GPR) approach to MOS

The GPR approach to MOS post-processing involves predicting the probability $p$ over daily precipitation $y$, conditional on a set of predictors $x$, using regression models with parameters $\phi$ and whose output variables characterise a stochastic process (Eq. 1). Importantly, we assume that the probability over daily precipitation at one spatio-temporal location is conditionally
150   independent from all other spatio-temporal locations, and thus the joint conditional probability $p(y|x)$ factorises into the product of $p(y_m|x_m)$, where $m$ ranges from 1 to $M$ and denotes a spatio-temporal location (i.e., there is a unique $m(s,t)$ for every combination of spatial location $s$ and time $t$).

$$p_\phi(y|x) = p_\phi(y_1, y_2, ..., y_m | x_1, x_2, ..., x_m) = \prod_{m=1}^{M} p_\phi(y_m|x_m). \tag{1}$$

More concretely, the GPR approach uses regression models $f_\phi$ that map from inputs $\mathbf{x}_m$ to outputs $\theta_m$ (Eq. 2). The input
155   vector $\mathbf{x}_m$ is $D$-dimensional, whereas the output vector $\theta_m$ is $N$-dimensional and it explicitly parametrises the conditional probability distribution over daily precipitation $y_m$. We use three regression model architectures, namely, vector generalised linear models (VGLMs; Song, 2007) and two fully-connected artificial neural networks, also referred to as multi-layer percep-trons (MLPs; Rumelhart et al., 1986).

$$\theta_m = f_\phi(\mathbf{x}_m). \tag{2}$$

160   In VGLMs, the mapping from inputs $\mathbf{x}_m$ to outputs $\theta_m$ in Eq. 2 involves two key transformations. Firstly, a linear transformation, parametrised by a matrix of weights $\mathbf{W}_1$, is applied to $\mathbf{x}_m$. Secondly, a non-linear transformation $\mathbf{g}$ is subsequently applied to obtain the output vector $\theta_m$. Note that each element $\theta_m^n$ is generated by applying a specific link function $g_n$, where $n$ ranges from 1 to $N$ and indexes each element of $\theta_m$ and $\mathbf{g}$. This element-wise non-linear transformation ensures that the resulting output values are valid parameters of the predicted probability distribution (Eq. 3).

165   $$\theta_m = \mathbf{g}(\mathbf{W}_1^\top \mathbf{x}_m). \tag{3}$$

Thus, for VGLMs, parameters $\phi = \mathbf{W}_1$.

In contrast, in MLPs the mapping from inputs $\mathbf{x}_m$ to outputs $\theta_m$ in Eq. 2 involves passing $\mathbf{x}_m$ through multiple hidden layers, in sequence. The mapping from each layer to the next layer involves several linear transformations (determined by the number of units in that layer and parametrised by matrices $\mathbf{W}_1, \mathbf{W}_2, ..., \mathbf{W}_{H+1}$, where $H$ is the number of layers), each followed by a
170   non-linear activation function $a$ (Eq. 4). This structure allows MLPs to model more complex (non-linear) relationships than a linear model. We use a very small MLP with one hidden layer of 10 units, where $\phi = \{\mathbf{W}_1, \mathbf{W}_2\}$ (Eq. 4; hereafter referred to as $\text{MLP}_\text{S}$) and a larger version with two hidden layers of 50 units each, where $\phi = \{\mathbf{W}_1, \mathbf{W}_2, \mathbf{W}_3\}$ (Eq. 5; hereafter referred to as $\text{MLP}_\text{L}$). Rectified linear unit (ReLU) non-linearities are used as hidden layer activations $a$ in both MLP architectures, except for the last layer, which also employs a vector of link functions $\mathbf{g}$ to map each output variable.

175   $$\theta_m = \mathbf{g}(\mathbf{W}_2^\top a(\mathbf{W}_1^\top \mathbf{x}_m)). \tag{4}$$

**Table 2.** Summary of variables used as inputs to the GPR post-processing models, grouped by variable type.

| Description | Acronym | Units |
|---|---|---|
| WRF liquid and total precipitation | RAIN, PRECIP | mm/day |
| WRF water vapour path | WVP | kg/m$^2$ (daily average) |
| WRF convective available potential energy | CAPE | m$^2$/s$^2$ (daily average) |
| WRF temperature daily avg, max, min, and range at 2 m | $T_{2m}$, $T_{2m,MAX}$, $T_{2m,MIN}$, $T_{2m,R}$ | K |
| WRF zonal and meridional wind at 10 m, 500 hPa, and 250 hPa | $U_{10m}$, $V_{10m}$, $U_{500}$, $V_{500}$, $U_{250}$, $V_{250}$ | m/s (daily average) |
| WRF vertical wind at 500 hPa and 250 hPa | $W_{500}$, $W_{250}$ | m/s (daily average) |
| WRF relative humidity at 2 m and 500 hPa | $RH_{2m}$, $RH_{500}$ | % (daily average) |
| WRF orography (based on surface geopotential height) | GPH | m |
| WRF land use index | LU | - |
| Latitude, longitude (of target station) | Y, X | m |
| Terrain elevation (of target station) | Z | m |
| Day of year encoded via sine and cosine functions | $DoY_{SIN}$, $DoY_{COS}$ | - |
| Year | Year | - |

$$\theta_m = \mathbf{g}(\mathbf{W}_3^\top a(\mathbf{W}_2^\top a(\mathbf{W}_1^\top \mathbf{x}_m))). \tag{5}$$

In order to post-process WRF daily precipitation outputs, the three GPR model architectures use an input vector $\mathbf{x}_m$ that consists of $D = 26$ variables listed in Table 2, i.e., resulting in a 26-dimensional vector. This includes outputs from the WRF simulation at some spatio-temporal location $m$, as well as other context variables relating to the geographical location, orography, and date. The outputs from the WRF simulation include daily precipitation (i.e., the variable that is being post-processed), as well as other variables that are closely related to precipitation, cloud properties, and convective processes, such as convective available potential energy, cloud water vapour path, relative humidity, horizontal and vertical winds, and temperature.

To characterise the conditional probability over daily precipitation, we employ a Bernoulli-gamma mixture model, which is capable of jointly accounting for precipitation occurrence and magnitude and has been used in previous studies (Williams, 1998; Cannon, 2008). Precipitation occurrence is modelled by introducing a Bernoulli random variable $r_m$, which takes the value 1 with probability $\pi_m$ and the value 0 with probability 1-$\pi_m$. When $r_m = 1$, precipitation magnitude $y_m$ is modelled by a gamma distribution with parameters $\alpha \in (0, \infty)$ and $\beta \in (0, \infty)$. The Bernoulli-gamma mixture is implemented by specifying regression models architectures that generate an $N = 3$ dimensional output vector $\theta_m = [\pi_m, \alpha_m, \beta_m]$, using link functions $\mathbf{g} = [\text{sigmoid}(\cdot), \exp(\cdot), \exp(\cdot)]$. Further implementation details can be found in Appendix A.

## 2.3 Training, validation and testing

The GPR post-processing models are trained, validated, and tested using the daily precipitation observations $y^{\text{obs}}$ (Table 1) as predictands, i.e., target values. We employ a k-fold cross-validation approach, which involves splitting the data by location (i.e., station) into $k$ folds, with $k-2$ folds being used for training, 1 fold for validating, and 1 fold for testing. This process is repeated $k$ times, ensuring each fold is used once for testing. During training, we optimise the model parameters $\phi$ to maximise the average log-likelihood of the training dataset. For this, we use stochastic gradient descent with a batch size of 128 and the Adam optimiser (Kingma and Ba, 2015) with an initial learning rate equal to $10^{-3}$. Here, we consider the validation step as part of the training process as it involves selecting, from the different model training iterations, the configuration of model parameters $\phi$ that maximises the average log-likelihood of the validation dataset, to avoid overfitting to the training data. We thus refer to the combined training and validation steps as training. Lastly, testing involves evaluating the performance of the trained models on the held-out locations in the test dataset.

## 2.4 Scaling factor approach

We compare the post-processed WRF precipitation results from the three GPR models against results using a widely-used deterministic MOS scaling factor approach (Maraun and Widmann, 2018), which we refer to as WRF$_{\text{SF}}$. Here, the raw WRF daily precipitation output for station $s$ (hereinafter referred to as $y_s^{\text{WRF}}$) is scaled by the ratio between total observed daily precipitation ($\sum_{m=1}^{M} y_m^{\text{obs}}$) and total WRF-simulated daily precipitation ($\sum_{m=1}^{M} y_m^{\text{WRF}}$), where data points indexed $m \in \{1, ..., M\}$ correspond to locations other than $s$, to obtain $y_s^{\text{WRF}_{\text{SF}}}$ (Eq. 6).

$$y_s^{\text{WRF}_{\text{SF}}} = y_s^{\text{WRF}} \left( \frac{\sum_{m=1}^{M} y_m^{\text{obs}}}{\sum_{m=1}^{M} y_m^{\text{WRF}}} \right). \tag{6}$$

The scaling factor method is also applied using a 10-fold spatial cross-validation approach, where the scaling factor is derived using $k = 9$ folds (i.e., data points indexed $m \in \{1, ..., M\}$) and then applied to the data points in the remaining fold.

## 2.5 Experiments

We undertake four experiments that assess the performance of the three GPR post-processing models, as well as the scaling factor approach WRF$_{\text{SF}}$. The four experiments represent increasingly complex (but realistic) ways of partitioning the available station data into subsets for training, validation, and testing, and are shown schematically in Fig. 2. In Experiment 1 (hereafter referred to as E1), we train separate GPR models for each region (i.e., separate-region models) and test them by post-processing the WRF precipitation output at held-out locations within that region. This experiment represents a baseline scenario, where models are trained and tested on the same region. In Experiment 2 (E2), we train GPR models using data from all three regions combined (i.e., a combined-region model) and test them by post-processing WRF precipitation output at held-out locations within each of the regions. This experiment therefore explores whether training a model over a diverse range of regions/settings and then applying it to each of these regions outperforms the separate-region (E1) models. Both E1 and E2 use

9

10-fold cross-validation. Experiment 3 (E3) is similar to E2 but trains and validates the models on combined data from two regions (consisting of 80% and 20% of the combined data, respectively), and tests on 100% of the data from a third, completely held-out, region. This experiment therefore explores whether a model that is trained over a set of regions/settings can generalise to an entirely different new region. In E3 we use 3-fold cross-validation to ensure that each region is held-out for testing once to

225 produce predictions for that region. Lastly, Experiment 4 (E4) is analogous to the separate-region (E1) experiment but splits the data up for training, validation, and testing based on the elevation of the stations. Here, for each region the top 10% elevation stations are withheld for testing, the next 10% are used for validation, and the remaining 80% (i.e., lowest elevation) stations are used for training. This experiment therefore explores whether models trained on data from the lower reaches of catchments, where the majority of stations are located, are capable of generalising to much higher elevations that are typically ungauged.

230 Note that E4 therefore does not involve k-fold cross-validation.

## 2.6 Evaluation metrics

To evaluate the post-processed precipitation distributions from each of the three GPR post-processing models in each of the three target regions, we employ three strictly proper scoring rules (Gneiting and Raftery, 2007), which are the negative log-likelihood (NLL), the continuous rank probability score (CRPS), and the Brier score (BS). For the CRPS and the BS, we

235 calculate their associated skill scores CRPSS and BSS, respectively (e.g., Angus et al., 2024). These measure the improvement relative to the CRPS and BS for the raw WRF precipitation output, which is considered as our baseline. The CRPSS and BSS metrics are also used to evaluate the skill of $\mathrm{WRF_{SF}}$.

The NLL assesses the compatibility of probabilistic hindcasts with observed data, especially focusing on the probability of observed events under the predicted probability distributions. It is defined as the sum of the natural logarithms of the probability

240 density function values at the observed data points (Eq. 7).

$$\mathrm{NLL} = -\frac{1}{M} \sum_{m=1}^{M} \log(p(y_m^{\mathrm{obs}}|x_m)), \tag{7}$$

where $M$ represents the number of observations, $y_m^{\mathrm{obs}}$ denotes the $m$-th observed data point, and $p(y_m^{\mathrm{obs}}|x_m)$ is the value of the predicted probability density function evaluated at that observed data point. NLL is the optimisation criterion used during training and therefore lower values indicate better performance.

245 The CRPS also measures how well probabilistic prediction matches the observed data $y_m^{\mathrm{obs}}$ by measuring the distance between the predicted and observed cumulative distribution functions (CDFs). The CRPS is defined as the integral of the squared difference between the predicted CDF $F(y_m)$ and the observed empirical CDF, which is the Heaviside step function $H(y_m - y_m^{\mathrm{obs}})$, over the entire range of possible values $y$ (Eq. 8).

$$\mathrm{CRPS} = \frac{1}{M} \sum_{m=1}^{M} \int_{-\infty}^{\infty} (F(y_m) - H(y_m - y_m^{\mathrm{obs}}))^2 dy_m. \tag{8}$$

250 Using this, the CRPSS is then calculated as:

$$\mathrm{CRPSS} = 1 - \frac{\mathrm{CRPS}}{\mathrm{CRPS_{WRF}}}, \tag{9}$$
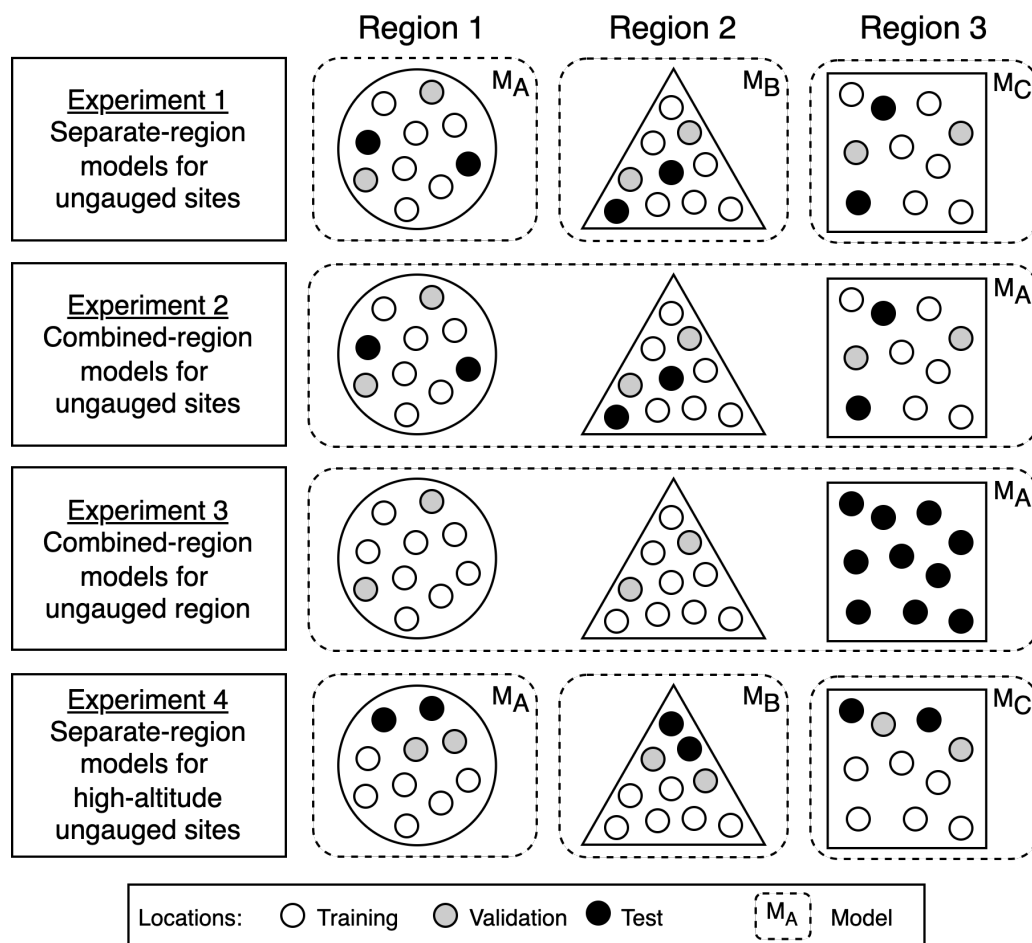
**Figure 2.** Schematic representation of the four experiments included in this study applied to three target regions. In Experiment 1, separate-region models for each of the three regions are trained and tested in held-out locations within each region. In Experiment 2, combined-region models are trained on data from all three regions and tested in held-out locations within those same regions. In Experiment 3, models are trained on two regions combined and tested in a third, completely held-out, region. Experiment 4 is analogous to Experiment 1 but held-out test locations are at higher elevations than those used for training and validation.

where $\text{CRPS}_{\text{WRF}}$ is the CRPS of the raw WRF precipitation output. Positive values of CRPSS indicate improved skill relative to the raw WRF output, with higher values indicating better performance. Note that for deterministic predictions (i.e., WRF and $\text{WRF}_{\text{SF}}$) the CRPS reduces to the mean absolute error between the predicted and observed values.

255    The BS (Wilks, 2006) measures the mean squared error between $M$ pairs of precipitation occurrence probabilities $\pi_m$ and binary observations $r_m^{\text{obs}}$ (Eq. 10). We compute the BS for various precipitation magnitude thresholds (0, 1, 10, 30 and 50 mm) that span the spectrum of precipitation events, ranging from no precipitation to very extreme events. This approach allows for a detailed assessment of the predictive capacity across different levels of precipitation intensity.

$$\text{BS} = \frac{1}{M} \sum_{m=1}^{M} (\pi_m - r_m^{\text{obs}})^2. \tag{10}$$

260    Using this, the BSS is calculated as:

$$\text{BSS} = 1 - \frac{\text{BS}}{\text{BS}_{\text{WRF}}}, \tag{11}$$

where $\text{BS}_{\text{WRF}}$ is the BS of the raw WRF precipitation output. Positive BSS values indicate an improved skill relative to the raw WRF output, with higher values indicating better performance.

We extend the performance assessment for the combined-region models (E2) as these showcase the benefits and challenges
265    associated with leveraging data from different regions. For this, we pool together the E2 held-out predictions for all (three) regions and use reliability diagrams and receiver operating characteristics (ROC) curves (e.g., Angus et al., 2024). Reliability diagrams serve as a visual representation of the calibration accuracy of predicted probabilities for different precipitation levels (0, 1, 10 and 30 mm/day), extending the evaluation beyond pairwise-correspondence metrics such as NLL, CRPSS and BSS. Reliability diagrams display the relationship between predicted probabilities of precipitation exceeding a certain threshold and
270    the actual observed frequencies, with a perfect agreement indicated by such relationship falling along the diagonal line on the graph. ROC curves offer an alternative perspective of probabilistic model performance across for different precipitation levels (0.1, 1, 10 and 30 mm/day). In particular, ROC curves assess the ability of probabilistic predictions to discriminate an event from a non-event by plotting the hit rate (i.e., ratio between the number of correctly predicted events and the total number of events) against the false alarm rate (i.e., ratio between the number of wrongly predicted events and the total number of events)
275    using different predicted probability thresholds to transform the probabilistic prediction into a binary prediction of occurrence (Wilks, 2006; Angus et al., 2024). To allow for a better graphical differentiation of the ROC curves for different precipitation events, data points with no observed precipitation are excluded from this analysis.

### 2.7    Feature ablation

To determine the most influential input variables for the three GPR post-processing models, we perform a feature ablation
280    analysis for E2 (Zeiler and Fergus, 2014; Kokhlikyan et al., 2020). Feature ablation is a technique that replaces each input variable (or feature) in $\mathbf{x}_m$ with a baseline value (in this case, zero) and measures the impact this has on the output vector $\theta_m$. This is done for each of the $D = 26$ input variables from Table 2 by running the trained GPR models 26 times, each time with a
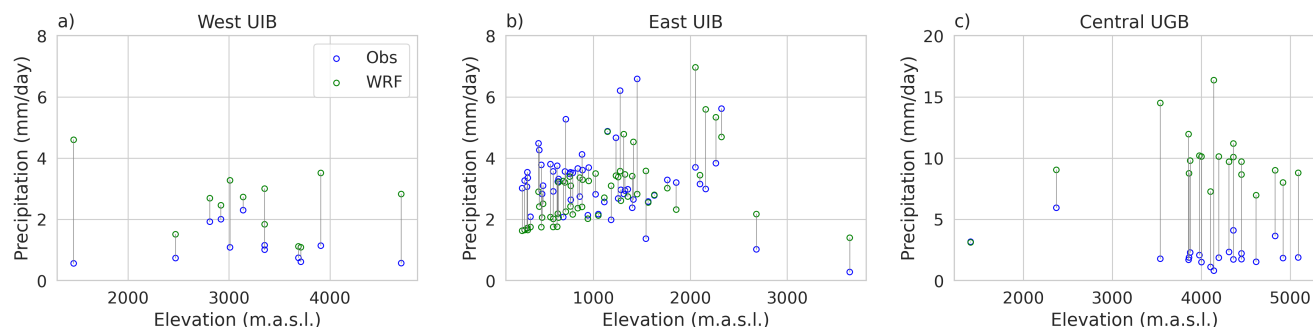
**Figure 3.** Difference between observed and WRF-simulated mean daily precipitation (mm/day) for each gauging station as a function of station elevation for a) West UIB, b) East UIB, and c) Central UGB.

different input variable in $\mathbf{x}_m$ replaced by zero, thereby obtaining predictions $\theta_m$ for each ablated-feature input configuration. For each feature, the average of the absolute value of the differences between the ablated-feature model predictions and the original model predictions is computed for each output variable, i.e., $\pi$, $\alpha$ and $\beta$.

## 3 Results

Figure 3 shows how differences between observed and WRF-simulated mean daily precipitation vary by region and with terrain elevation. In West UIB and Central UGB, WRF systematically overestimates precipitation for all stations, i.e., for the full elevation range of the stations. This overestimate is especially apparent in Central UGB, with station measurements showing values of around 2 mm/day, whereas WRF generally simulates 8-10 mm/day. In East UIB, WRF underestimates precipitation at low-elevation stations (below around 1000 m.a.s.l.) and broadly overestimates it at higher elevations (especially above 2000 m.a.s.l.). These results generally show that the WRF output is characterised by highly variable precipitation biases across the three target regions that are consistent with complex elevation and hydro-climatological dependencies, and therefore that generalising MOS post-processing at ungauged locations is likely challenging.

Table 3 evaluates the performance of the three GPR post-processing models (VGLM, MLP$_S$ and MLP$_L$) for each experiment and region using NLL. For E1, which assesses separate-region models for each of the three target regions, both MLP models marginally outperform the VGLM model in all three regions, with MLP$_L$ performing best. Similar results are also apparent for E2, which tests how combined-region models generalise to held-out locations within those regions. Comparison of E2 and E1 shows that the combined-region GPR models (E2) perform marginally better than the separate-region GPR models (E1) for East UIB, but are marginally poorer for West UIB and Central UGB. However, the NLL values for E1 and E2 for each region and each GPR model are very similar and only differ in the second decimal place, i.e., there is little difference between the performance of either the separate-region or combined-region models, as well as between the three GPR models. For E3, which is analogous to E2 but the GPR models are trained using data from two regions combined together and tested on the third

13

region, NLL values are much higher compared to E2, highlighting a considerable drop in performance in all three regions. For example, the NLL value for $MLP_L$ for West UIB is 1.24 for E2 and 2.46 for E3. Additionally, in E3, the range of NLL values within each region is relatively wide compared to E2, indicating that GPR performance in E3 is more sensitive to the choice of model architecture. For example, for West UIB the NLL value is 1.50 for VGLM, 2.84 for $MLP_S$, and 2.46 for $MLP_L$. For E4, which is analogous to E1 but testing happens at locations with higher elevations than those seen by the models during training, the performance of all GPR models slightly drops compared to E1. However, the NLL values for E1 and E4 for West UIB and East UIB still only differ in the second decimal place. Here, $MLP_S$ shows the best performance for West UIB and East UIB, while for Central UGB it is $MLP_L$.

In terms of differences across all experiments and models for each region, NLL values in East UIB are lower than those in West UIB by around 0.1, while NLL values in West UIB are in turn lower than those in Central UGB by (typically) 0.2 to 0.3 (Table 3). This pattern highlights the dominance of regional variability, driven by the quality/bias of the raw WRF output and the amount of station data available. For example, East UIB has the best-performing models and also the highest number of daily precipitation measurements (364,713), with West UIB having the second best-performing models and also the second highest number of measurements (76,860), and finally Central UGB has the poorest performing models and also the least number of measurements (15,152) (Table 1).

**Table 3.** NLL values of post-processed daily WRF precipitation for the three GPR model architectures (VGLM, $MLP_S$ and $MLP_L$), calculated for all four experiments and all three target regions. Lower NLL values indicate better performance, with the best-performing GPR model for each experiment and region shown in bold. NLL values are directly comparable across experiments and regions. Note that $MLP_L$ for E3 West UIB was trained using a learning rate of $10^{-4}$ to ensure training convergence, while the other experiments used $10^{-3}$.

| Experiment | West UIB | | | East UIB | | | Central UGB | | |
|---|---|---|---|---|---|---|---|---|---|
| | VGLM | $MLP_S$ | $MLP_L$ | VGLM | $MLP_S$ | $MLP_L$ | VGLM | $MLP_S$ | $MLP_L$ |
| E1 | 1.263 | 1.235 | **1.226** | 1.179 | 1.159 | **1.150** | 1.480 | 1.437 | **1.420** |
| E2 | 1.267 | 1.245 | **1.240** | 1.181 | 1.156 | **1.144** | 1.501 | 1.477 | **1.448** |
| E3 | **1.502** | 2.835 | 2.457 | 2.414 | 1.531 | **1.483** | **1.683** | 1.985 | 1.950 |
| E4 | 1.283 | **1.250** | 1.251 | 1.187 | **1.160** | 1.173 | 1.875 | 1.553 | **1.511** |

Table 4 extends the performance assessment by showing the CRPSS for the three GPR models. The CRPSS values are largely consistent with the NLL results. For example, both MLP models outperform VGLM in all three regions for E1 and E2, and $MLP_L$ is the best overall performing model. The CRPSS values for E1 and E2 for each region are very similar and only differ in the second decimal place, which was also found for the NLL results. For E3, all three GPR models exhibit lower CRPSS values and larger differences between models compared to E2, i.e, consistent with the considerable performance drop in all three regions and a higher sensitivity to the choice of model architecture found by NLL results. However, as CRPSS values for the GPR models are relative to the reference $CRPS_{WRF}$, the positive CRPSS values achieved still represent an improvement in skill relative to WRF. For E3, $MLP_S$ performs best for West UIB and East UIB (in contrast to VGLM for West UIB and

$MLP_L$ for East UIB for the NLL results), while VGLM performs best for Central UGB (in agreement with the NLL results). For E4, the performance of all models slightly drops compared to E1, with the $MLP_L$ model still performing best across all three regions (in contrast to $MLP_S$ for West UIB and East UIB for the NLL results, but in agreement with $MLP_L$ for Central

330     UGB, for the NLL results). CRPSS values also display differences across all experiments and models for each region, with the highest values of around ∼0.8 in Central UGB, followed by values of ∼0.6 for West UIB, and finally ∼0.4 for East UIB. However, as CRPSS values are relative to (and thus influenced by) $CRPS_{WRF}$, which varies for each region, they are therefore not directly comparable across regions.

Table 4 also shows CRPSS values for $WRF_{SF}$. For all experiments and regions, the CRPSS values for $WRF_{SF}$ are lower
335     than those for the GPR models, indicating that the performance of the GPR models is superior to $WRF_{SF}$. For example, for E1 and E4 the $WRF_{SF}$ values for East UIB are close to zero (-0.07), but positive in West UIB (∼0.4) and Central UGB (0.69), i.e., indicating negligible improvement relative to the raw WRF output for East UIB, but some improvement for West UIB and Central UGB. This is likely related to the direction of WRF-simulated biases changing with elevation for East UIB, while for West UIB and Central UGB the biases are larger unidirectional (Fig. 3), i.e., large and unidirectional biases are more easily
340     post-processed and thus the scaling factor approach is also effective. For E2, $WRF_{SF}$ exhibits CRPSS values close to zero, indicating negligible improvement relative to the raw WRF output. For E3, $WRF_{SF}$ shows values close to zero for West UIB (-0.03) and Central UGB (-0.04), but positive values for East UIB (0.35).

**Table 4.** CRPSS values of post-processed daily WRF precipitation for the three GPR model architectures (VGLM, $MLP_S$ and $MLP_L$) and $WRF_{SF}$, calculated for all three regions and all four experiments. Higher CRPSS values indicate better performance, with the best-performing MOS method for each experiment and region shown in bold. Positive CRPSS values indicate improved skill relative to raw WRF hindcasts. CRPSS values are directly comparable across experiments but not across regions.

| Experiment | West UIB | | | | East UIB | | | | Central UGB | | | |
|---|---|---|---|---|---|---|---|---|---|---|---|---|
| | VGLM | $MLP_S$ | $MLP_L$ | $WRF_{SF}$ | VGLM | $MLP_S$ | $MLP_L$ | $WRF_{SF}$ | VGLM | $MLP_S$ | $MLP_L$ | $WRF_{SF}$ |
| E1 | 0.646 | 0.654 | **0.657** | 0.397 | 0.416 | 0.433 | **0.434** | -0.075 | 0.820 | 0.823 | **0.824** | 0.691 |
| E2 | 0.645 | 0.647 | **0.652** | 0.021 | 0.416 | 0.428 | **0.439** | 0.022 | 0.814 | 0.811 | **0.825** | 0.043 |
| E3 | 0.491 | **0.585** | 0.556 | -0.027 | 0.346 | **0.384** | 0.354 | 0.234 | **0.812** | 0.779 | 0.782 | -0.039 |
| E4 | 0.625 | 0.628 | **0.644** | 0.398 | 0.414 | 0.427 | **0.430** | -0.073 | 0.808 | 0.818 | **0.818** | 0.690 |

To better understand the performance of the GPR models for various precipitation intensities, Table 5 shows the BSS for the three GPR models for different daily precipitation thresholds. As expected, BSS values are consistent with CRPSS results but provide further granularity. For E1, E2 and E4, $MLP_L$ is best at capturing the probability over low-to-moderate precipitation
345     thresholds (i.e., 0, 1 and 10 mm/day), whereas results for higher precipitation events (i.e., 30 and 50 mm/day) are variable. However, for each region and threshold the BSS values for different models generally only differ in the second decimal place, indicating that the performance of all GPR models is broadly similar for each region and threshold. For a threshold of 50 mm/day, smaller models generally perform marginally better for E1 (i.e., $MLP_S$ in West UIB and East UIB, and VGLM in

350 Central UGB), E3 ($MLP_S$), and E4 (VGLM), whereas $MLP_L$ performs best in E2 for East UIB and Central UGB. For E3, the VGLM model considerably outperforms the MLP models for low precipitation thresholds (i.e., 0 and 1 mm/day) in West UIB and Central UGB, whereas $MLP_S$ performs best for higher thresholds (i.e., 30 and 50 mm/day) in these regions. Moreover, E3 also shows a much wider difference between models for West UIB and Central UGB. For example, for West UIB and a threshold of 30 mm/day, the BSS value is 0.47 for VGLM, 0.74 for $MLP_S$, and 0.68 for $MLP_S$.

355 For all experiments and regions, the BSS values for $WRF_{SF}$ are generally much lower than for the GPR models, indicating that the performance of the GPR models is superior to $WRF_{SF}$ (i.e., consistent with the CRPSS results). However, for E1 and E4, $WRF_{SF}$ can have BSS values that are comparable to the GPR models for higher thresholds, especially for East UIB and Central UGB. For example, for Central UGB the BSS value for a threshold of 50 mm/day is 0.91 for $MLP_L$ and 0.90 for $WRF_{SF}$.

360 Figure 4 shows reliability diagrams and corresponding observed precipitation event histograms for daily precipitation thresholds exceeding 0, 1, 10 and 30 mm/day for E2, i.e., the combined-region model. For low precipitation thresholds (i.e., 0 and 1 mm/day) the reliability diagrams show that the majority of predicted probabilities are well-calibrated (Fig. 4(a,b)), which is indicated by the data points corresponding analogous levels to predicted probability and observed frequency of precipitation (dashed line) coinciding with the diagonal line (solid line). However, the calibration accuracy declines for predicted probability

365 values of between 0.9 and 1.0 due to the model overpredicting the observed frequency. This occurs when the count of predicted instances for a given cumulative probability value decreases below a threshold of around $10^3$ (Fig. 4(e,f)). This effect is even more evident for higher precipitation thresholds (i.e., 10 and 30 mm/day), where predicted probabilities and observed frequencies start to deviate at around 0.5 and 0.2, respectively (Fig. 4(c,d)), due to the model overpredicting the observed frequency. This also coincides with the number of predicted instances for these higher precipitation events dropping below a threshold of

370 around $10^3$ (Fig. 4(g,h)), which highlights the challenge of predicting extreme precipitation events.

Figure 5 displays ROC curves for daily precipitation thresholds exceeding 0.1, 1, 10 and 30 mm/day for E2. This shows that GPR models exhibit superior binary classification accuracy compared to raw WRF and $WRF_{SF}$ for all precipitation thresholds. This is graphically depicted in Fig. 5 by the (probabilistic) curves sitting considerably above the (deterministic) point values in the diagrams, indicating that the GPR models have higher true hit rate at equivalent or lower false alarm rates compared

375 to WRF and $WRF_{SF}$. Such a consistent pattern reinforces the evidence that GPR models not only provide a more nuanced forecast by quantifying uncertainty but also deliver a more reliable prediction in terms of discriminating between events and non-events for a given daily precipitation threshold. Additionally, Fig. 5 also shows for all precipitation thresholds that $MLP_L$ consistently yields the best performance of the GPR models. Note that ROC diagrams in Fig. 5 exclude data points with no observed precipitation (i.e., dry days) from the analysis.

380 Figure 6 shows the effect that progressively adding input variables (listed in Table 2) has on GPR model performance for E2, in particular on the held-out NLL value for $MLP_L$. Starting with a set of core input variables (i.e., PRECIP, RAIN, $DOY_{SIN}$, $DOY_{COS}$ and Z), the $MLP_L$ model yields a held-out NLL value of 1.33 (configuration labelled 'Core variables' in Fig. 6). By comparison, adding the spatial variables LAT and LON to the core set yields a held-out NLL value of 1.24 (labelled '+ Spatial variables'), while further adding the vertically-integrated thermodynamic/cloud related input variables WVP and CAPE to this

**Table 5.** BSS values of post-processed daily WRF precipitation for the three GPR model architectures (VGLM, MLP$_S$ and MLP$_L$) and WRF$_{SF}$, calculated for all three regions and all four experiments using a range of daily precipitation thresholds (0, 1, 10, 30 and 50 mm/day). Higher BSS indicate better performance, with the best-performing MOS method for each experiment and region shown in bold. Positive BSS values indicate improved skill relative to raw WRF hindcasts. BSS values are directly comparable across experiments but not across regions.

| E | T (mm) | West UIB | | | | East UIB | | | | Central UGB | | | |
|---|---|---|---|---|---|---|---|---|---|---|---|---|---|
| | | VGLM | MLP$_S$ | MLP$_L$ | WRF$_{SF}$ | VGLM | MLP$_S$ | MLP$_L$ | WRF$_{SF}$ | VGLM | MLP$_S$ | MLP$_L$ | WRF$_{SF}$ |
| E1 | 0 | 0.528 | 0.544 | **0.550** | 0.000 | 0.520 | 0.548 | **0.559** | 0.000 | 0.515 | 0.522 | **0.537** | 0.000 |
| E1 | 1 | 0.484 | 0.502 | **0.511** | 0.110 | 0.390 | 0.426 | **0.441** | -0.010 | 0.582 | 0.595 | **0.615** | 0.142 |
| E1 | 10 | 0.748 | **0.753** | **0.753** | 0.554 | 0.403 | 0.425 | **0.428** | -0.035 | 0.823 | 0.829 | **0.830** | 0.699 |
| E1 | 30 | 0.746 | **0.752** | 0.744 | 0.667 | 0.448 | **0.456** | 0.451 | -0.111 | **0.934** | 0.932 | 0.926 | 0.929 |
| E1 | 50 | 0.686 | **0.692** | 0.680 | 0.667 | 0.461 | **0.465** | 0.457 | -0.143 | **0.914** | 0.911 | 0.907 | 0.903 |
| E2 | 0 | 0.528 | 0.529 | **0.538** | 0.000 | 0.524 | 0.550 | **0.561** | 0.000 | 0.474 | 0.497 | **0.522** | 0.000 |
| E2 | 1 | 0.493 | 0.492 | **0.496** | 0.004 | 0.397 | 0.426 | **0.441** | 0.005 | 0.545 | 0.560 | **0.597** | 0.006 |
| E2 | 10 | 0.747 | 0.748 | **0.752** | 0.024 | 0.404 | 0.419 | **0.433** | 0.012 | 0.820 | 0.810 | **0.825** | 0.020 |
| E2 | 30 | 0.741 | **0.750** | 0.748 | 0.054 | 0.443 | 0.450 | **0.458** | 0.027 | **0.938** | 0.937 | **0.938** | 0.086 |
| E2 | 50 | 0.679 | **0.692** | 0.672 | 0.060 | 0.457 | 0.461 | **0.465** | 0.0048 | 0.917 | 0.917 | **0.919** | 0.101 |
| E3 | 0 | **0.519** | 0.299 | 0.308 | 0.000 | 0.427 | **0.458** | 0.442 | 0.000 | **0.418** | 0.051 | 0.117 | 0.000 |
| E3 | 1 | **0.485** | 0.331 | 0.338 | -0.005 | 0.263 | **0.340** | 0.314 | 0.054 | **0.534** | 0.318 | 0.360 | -0.003 |
| E3 | 10 | 0.471 | **0.741** | 0.728 | -0.028 | 0.326 | **0.375** | 0.329 | 0,172 | **0.817** | 0.811 | 0.808 | -0.024 |
| E3 | 30 | 0.473 | **0.745** | 0.680 | -0.060 | 0.400 | **0.416** | 0.399 | 0.341 | 0.934 | **0.939** | 0.936 | -0.074 |
| E3 | 50 | 0.516 | **0.686** | 0.483 | -0.090 | 0.432 | **0.438** | 0.431 | 0.410 | **0.916** | **0.916** | 0.912 | -0.099 |
| E4 | 0 | 0.521 | 0.534 | **0.546** | 0.000 | 0.519 | 0.544 | **0.555** | 0.000 | 0.441 | 0.461 | **0.501** | 0.000 |
| E4 | 1 | 0.458 | 0.486 | **0.504** | 0.110 | 0.390 | 0.422 | **0.432** | -0.010 | 0.566 | 0.556 | **0.577** | 0.142 |
| E4 | 10 | 0.732 | 0.720 | **0.736** | 0.554 | 0.400 | 0.418 | **0.422** | -.0.035 | 0.806 | 0.824 | **0.826** | 0.688 |
| E4 | 30 | 0.741 | 0.728 | **0.743** | 0.667 | 0.444 | 0.448 | **0.449** | -0.111 | 0.938 | **0.939** | 0.932 | 0.926 |
| E4 | 50 | **0.683** | 0.669 | **0.683** | 0.667 | **0.460** | 0.458 | 0.459 | -0.143 | **0.916** | **0.916** | 0.908 | 0.903 |
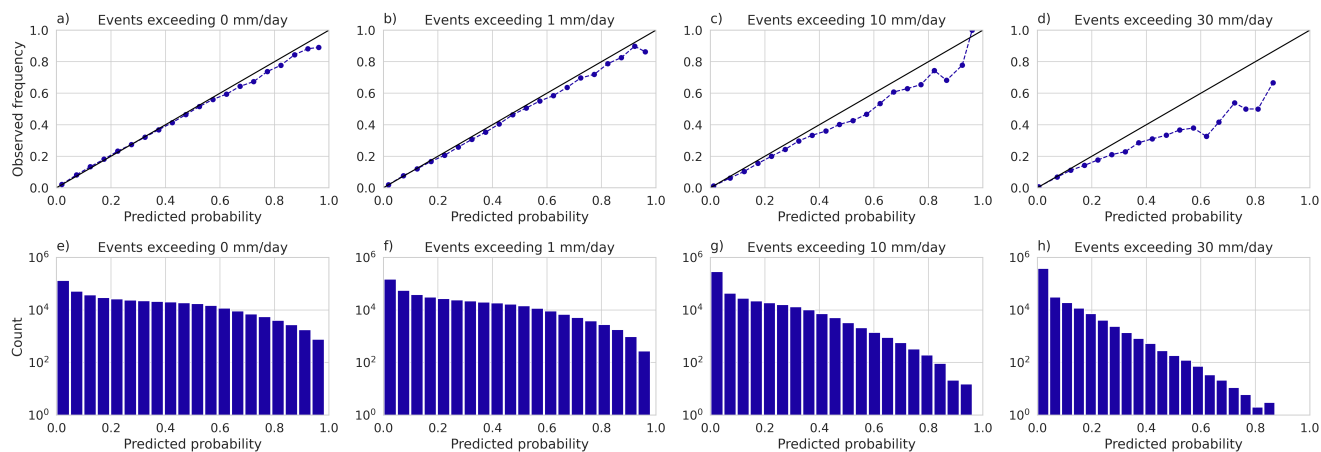
**Figure 4.** Reliability diagrams (top panels) and predicted probability histograms (bottom panels) for different observed daily precipitation thresholds of 0.1 mm/day (a,e), 1 mm/day (b,f), 10 mm/day (c,g), and 30 mm/day (d,h). Reliability diagrams (a,b,c,d) display the relationship between predicted probabilities and the actual observed frequencies of precipitation exceeding a certain threshold (dotted line), with a perfect agreement indicated by the diagonal line (solid line). Predicted probability histograms (e,f,g,h) display the counts of observed events exceeding a certain threshold associated with various predicted probability levels.
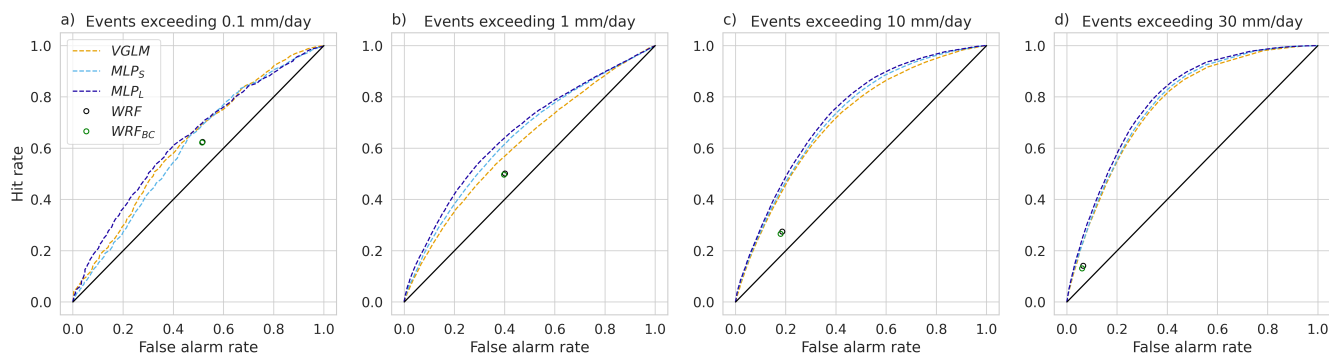


**Figure 5.** Receiver Operating Characteristic (ROC) curves yielded by the three GPR models, as well as hit rate and false alarm rate for WRF and WRF$_{SF}$, for different daily precipitation thresholds of 0.1 mm/day (a), 1 mm/day (b), 10 mm/day (c), and 30 mm/day (d). ROC curves exclude data points with no observed precipitation.

| Configuration | Additional input variables | Test NLL |
|---|---|---|
| Core variables | PRECIP, RAIN, $DOY_{SIN}$, $DOY_{COS}$, Z | 1.325 |
| + Spatial variables | LAT, LON | 1.237 |
| + Integrated variables | CAPE, WVP | 1.202 |
| + Temperature variables | $T_{2m}$, $T_{2m,MAX}$, $T_{2m,MIN}$, $T_{2m,R}$ | 1.197 |
| + Wind variables | $U_{10m}$, $V_{10m}$, $U_{500}$, $V_{500}$, $U_{250}$, $V_{250}$, $W_{500}$, $W_{250}$ | 1.195 |
| + Relative humidity vars. | $RH_{2m}$, $RH_{500}$ | 1.181 |
| + All other variables | GPH, LU, YEAR | 1.179 |
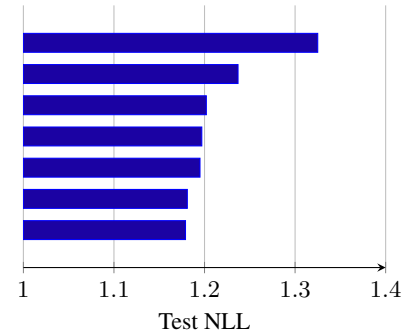
**Figure 6.** Test NLL yielded by $MLP_L$ in E2 for different configurations of input variables. Each configuration includes all the input variables from the preceding rows in addition to the specific set of input variables listed for that configuration. For example, the configuration labelled 'Core variables' contains the input variables PRECIP, RAIN, $DOY_{SIN}$, $DOY_{COS}$ and Z, whilst the configuration labelled '+ Spatial variables' contains 'Core variables' plus LAT and LON.

385    configuration yields a value of 1.20 (labelled '+ Integrated variables'), i.e, indicating a systematic improvement in skill as the number of input variables increases. However, adding the temperature-related input variables $T_{2m}$, $T_{2m,MAX}$, $T_{2m,MIN}$ and $T_{2m,R}$ (labelled '+ Temperature variables'), and then further adding the horizontal and vertical wind-related input variables $U_{10m}$, $V_{10m}$, $U_{500}$, $V_{500}$, $U_{250}$, $V_{250}$, $W_{500}$, and $W_{250}$ (labelled '+ Wind variables'), results in held-out NLL values of 1.20, i.e., indicating negligible gain in skill compared to the '+ Integrated variables' configuration. By contrast, adding the relative

390    humidity variables $RH_{2m}$ and $RH_{500}$ further reduces the held-out NLL value to 1.18, which is likely due to these input variables being thermodynamic/cloud related. Lastly, adding the remaining input variables GPH (i.e., WRF orography), LU and YEAR yields a held-out NLL value of 1.18, i.e., no significant improvement.

   Figure 7 assesses the relative influence that the input variables listed in Table 2 have on predicted outputs (i.e., the distributional parameters $\theta$, $\alpha$ and $\beta$) for the three GPR model architectures in E2. The feature importance analysis shows that the

395    VGLM model is heavily influenced by a relatively limited set of input variables, whereas the MLP models (in particular $MLP_L$) leverage a more extensive array of predictors. The set of influential input variables is moderately consistent for all three output parameters. However, one notable exception is the dominant effect that $T_{2m}$ has on $\pi$ (Fig. 7a), but not on $\alpha$ and $\beta$ (Fig. 7(b,c)), for the VGLM model. The results further show that, for all three GPR models, the vertically-integrated thermodynamic/cloud variables (CVW and CAPE), the relative humidity variables ($RH_{2m}$ and $RH_{500}$), and the near-surface temperature variables

400    ($T_{2m}$, $T_{2m,MAX}$, $T_{2m,MIN}$ and $T_{2m,R}$), stand out as important features, as well as inputs such as LAT, Z, and GPH. Moreover, and perhaps surprisingly, the precipitation input variables PRECIP and RAIN exhibit minimal influence on the GPR model outputs, which likely also explains the importance of the vertically-integrated thermodynamic/cloud variables and the relative humidity variables, as these play a dominant role in controlling precipitation. Furthermore, the contribution of the horizontal and vertical wind velocity fields to the GPR outputs is also relatively minor. It is important to note that this feature ablation analysis does

405    not assess multivariate effects, but only the effect that removing a single input variable (i.e., replacing it with zeros) has on the

**19**
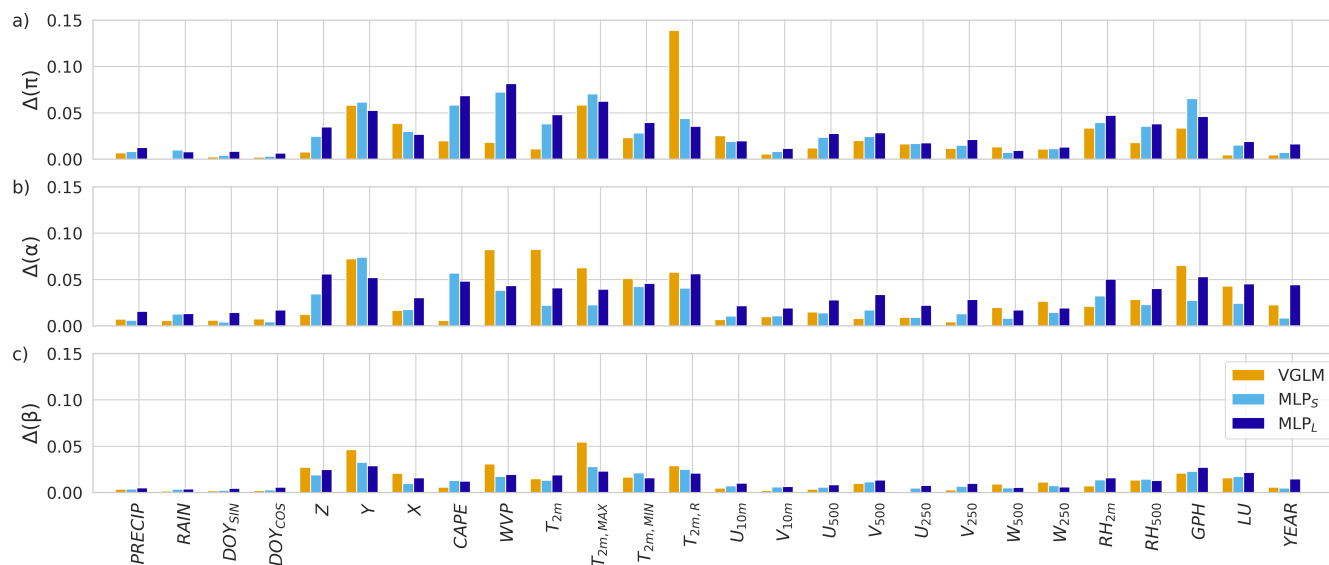
**Figure 7.** Feature ablation analysis for the three GPR models for E2, showing the effect that removing each input variable has on the output distributional parameters $\pi$ (a), $\alpha$ (b), and $\beta$ (c). Each vertical bar shows the average absolute-value output shift caused by ablating (i.e., replacing by zeros) a specific input variable, i.e., the larger the bar the more important the input variable is to the model.

GPR model outputs. As a result, the lack of influence shown by certain variables could be due to these being redundant given all other input variables (as evident in Fig. 6).

## 4 Discussion

In this study, we have shown that using a GPR approach to MOS post-process (i.e., downscaling and bias-correcting) daily
410 precipitation output from a reanalysis-driven RCM, for which simulated and observed daily precipitation are expected to exhibit pairwise correspondence, improves predictions at ungauged locations across all tested regions, precipitation thresholds, and experiments. We use three scoring metrics (NLL, CRPSS and BSS) to evaluate the quality of hindcasts and find that, overall, the three GPR models we employ (VGLM, $MLP_S$, and $MLP_L$) exhibit similar performance (Tables 3, 4, 5) and consistently yield superior skill relative to the raw RCM output (WRF) and deterministic MOS bias correction ($WRF_{SF}$) (Tables 4, 5). We find
415 that NLL (Table 3) and CRPSS (Table 4) yield similar relative rankings of GPR model performance. This is not surprising given that both the NLL and CRPS are strictly proper scoring rules that assess the goodness of fit of a predictive distribution against, in our case, a single observation, and have their minimums at the same value. However, the NLL is much more sensitive to extreme cases (as it involves a harsh penalty for events with low predicted probabilities) than the CRPS (Gneiting and Raftery, 2007). Therefore, it is insightful to corroborate the consistency of performance by using both scoring rules, whilst also noting
420 that using the CRPS as the optimisation criterion for the GPR model parameters would have resulted in different GPR models and associated predictions. The BS assesses the accuracy of probabilistic predictions specifically for binary events. Whilst the

CRPS is the integral of the BS over all real-valued probability thresholds and can therefore be viewed as a generalisation of the latter (Gneiting and Raftery, 2007), calculating the BS for specific precipitation thresholds provides additional granularity and shows insightful patterns for extreme precipitation events (Table 5).

425     MOS post-processing of RCM daily precipitation outputs at ungauged locations involves using separate groups of stations for model training, validation and testing. However, given the high spatial variability that daily precipitation exhibits both within and across regions, such an approach involves testing on out-of-distribution data, that is, models are assessed on their ability to generalise to held-out data that significantly deviates from the training data. This presents a particular challenge to representing extreme precipitation events. Daily precipitation in the three target regions is heavily skewed towards dry and

430     very-low precipitation amounts, with high-intensity precipitation events accounting for a very low fraction of the data (not shown). This imbalance hinders the models' ability to learn a robust representation of the probabilities associated with extreme precipitation events, and how these vary spatially and temporally. For instance, the smaller / simpler GPR models such as VGLM and $MLP_S$ stand out as more robust options for extreme precipitation events (Table 5), which is likely because they have fewer trainable parameters, and are thus able to learn less intricate patterns from the training data.

435     The four experiments we perform in this study assess GPR model performance across different post-processing tasks, which involve different ways of splitting data into training, validation and test sets. The dependencies between the training, validation and test datasets vary widely depending on whether the task involves a single region (E1) or multiple combined regions (E2), or extrapolating to either new regions (E3) or high elevations (E4). This explains the need for training models specific to each experiment and also highlights the spread of post-processing tasks considered in this work, attempting various degrees of

440     generalisation. Consequently, the properties of the models trained to perform each task will also be different, which explains why GPR models ranked differently depending on the experiment.

In comparing GPR model performance across experiments, we showed that combined-region GPR models (E2) result in marginally better predictions than separate-region models (E1) for East UIB (Tables 3 and 4). Here, we hypothesise that East UIB benefits from combining data from all three regions because of the inherent challenges of this region, which is

445     characterised by a complex bias-elevation distribution (Fig. 3), as well as an under-representation of station data at high elevations bands (>2,500 m.a.s.l., Fig. 1). We also find that GPR models are capable of improving daily precipitation hindcasts in completely ungauged regions (E3) by leveraging data from other regions (Tables 4 and 5). This result contradicts with the assumption that because RCM daily precipitation biases are region-specific (Maussion et al., 2011; Norris et al., 2017; Bannister et al., 2019; ul Hasson et al., 2019), they are therefore not easily-transferable to other regions. It is likely that GPR

450     models are partially able to overcome this issue because, conditional on enough information (i.e., relevant input features), daily precipitation biases for different regions share some similarities. E4 explores GPR model generalisation to locations situated at higher elevations than the gauging stations used to train the models. We find that GPR models successfully post-process WRF precipitation for all regions and thresholds, exhibiting only a marginal performance drop relative to E1 (Tables 3, 4, 5). This findinzg is particularly important given that much of the high elevation regions of HKH suffer from a profound lack of gauges

455     (Pritchard, 2021; Thornton et al., 2022; Krishnan et al., 2019).

21

We find that training GPR models with progressively richer predictor configurations (i.e., with additional input variables, see Table 2) has a consistently positive effect on model performance, with some input variables (e.g., spatial, vertically-integrated, and relative humidity variables) driving most of the performance improvement (Fig. 6). Notwithstanding this, the performance gain yielded by incorporating additional input variables is strongly dependent on the previously added input variables. Thus,

460    the relatively minor beneficial effect of variables such as temperatures and winds is likely only highlighting some degree of redundancy in the signal provided by different input variables. Furthermore, the three GPR models respond differently to the ablation of single input variables (Fig. 7), which highlights the complex interplay between input variables and model architecture. The reliance of the VGLM model architecture on a few input features contrasts the broader utilisation of inputs necessary for the $MLP_L$ model. The influence exhibited by input variables such as elevation and latitude (i.e., representing topography),

465    and convective available potential energy (CAPE), wave vapour, and relative humidity (i.e., representing thermodynamics) for post-processing daily precipitation is in line with findings from previous studies showing that precipitation in this region is strongly associated with thermodynamical and dynamical interactions with topography (Orr et al., 2017; Potter et al., 2018; Bannister et al., 2019; Medina et al., 2010; Ramezani Ziarani et al., 2019; Dimri et al., 2017). In contrast, somewhat surprisingly, input variables such as total and liquid precipitation have little influence on output values (Fig. 7), which we hypothesise

470    is partly due to the redundancy that exists between input variables, which in turn enables GPR models to compensate for the ablation of a single input variable by leveraging other variables.

## 4.1 Necessity for probabilistic predictions

Probabilistic and deterministic predictions are inherently different and it is important to consider this when evaluating the quality of the products produced by both types of models. In this work, we are interested in assessing the performance of

475    (probabilistic) GPR models, which leverage the pairwise correspondence between WRF daily precipitation output and observations, whilst capturing the predictive uncertainty that arises from multiple sources. A probabilistic MOS approach is justified if the goal is to fully leverage the richer predictions yielded by these models. For example, GPR model predictions can be used to map probabilities of exceedance for different precipitation events (Fig. 8(a,b,c)), which form the basis of risk assessments, or in downstream impact modelling settings that are capable of leveraging probability distributions over precipitation. The latter is

480    an emerging and largely untapped area of research for many impact modelling fields reliant on precipitation as one of the main inputs (e.g., hydrological and crop modelling; Li et al., 2013; Peleg et al., 2017). Conversely, if the intended use of the models is to essentially reduce the probabilistic predictions into a deterministic product, then deterministic metrics should be used to evaluate them. To this end, we use ROC curves to show that, for different precipitation thresholds, deterministic projections of GPR predictions still consistently outperform WRF and $WRF_{SF}$ (Fig. 5).

485    Accurate representation of past and present-day daily precipitation holds significant importance for various downstream tasks, such as hydrological modelling, crop modelling, or hazard analysis, all of which heavily rely on the hindcast precipitation for calibration. In hydrological modelling, knowing the distribution and timing of daily precipitation is crucial for simulating streamflow and predicting river flooding events (e.g., Andermann et al., 2011; Huang et al., 2019; Li et al., 2017; Wulf et al., 2016). Similarly, in crop modelling, precise knowledge of daily precipitation patterns enables accurate estimation of water
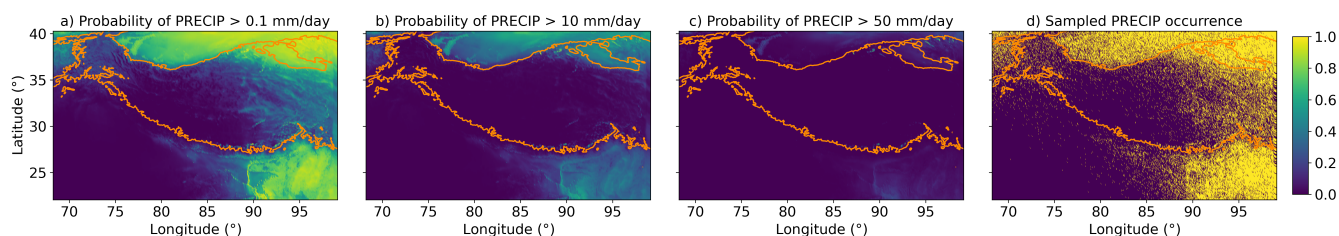
**Figure 8.** Panels a), b), and c) show maps showing the probability of precipitation exceeding 0.1 mm/day (a), 10 mm/day (b) and 50 mm/day (c) over the entire WRF spatial domain on an arbitrary date (10/10/2010) using the $MLP_L$ post-processing model trained using one of the k-fold splits in E2. Panel d) shows a map of modelled precipitation occurrence based on independently drawn samples from each grid-cell's predicted probability distribution for the entire WRF spatial domain on an arbitrary date (01/01/2010) using the $MLP_L$ post-processing model trained using one of the k-fold splits in E2. The 3000 m.a.s.l. contour is shown in orange in all four maps.

490     availability and crop growth, leading to improved yield predictions and agricultural management decisions (De Wit et al., 2005). In hazard analysis, past climate data is paired with historic events (e.g., glacial lake outburst floods; Shrestha et al., 2023) to be able to determine what precipitation intensity triggered them.

### 4.2    Limitations and future work

Local-scale variability of precipitation in HKH remains a challenge for MOS post-processing models aimed at ungauged
495     locations. The diverse climatic conditions and complex terrain in the region result in contrasting precipitation patterns among nearby stations, which limits the degree to which patterns observed in one location are representative of nearby locations (Immerzeel et al., 2014; Orr et al., 2017; Bhardwaj et al., 2021; Ren et al., 2017; Dimri et al., 2017; Thayyen et al., 2013; Potter et al., 2018). Using different locations to train, validate and test models is a common strategy in spatial prediction settings but it can introduce model biases (Burt et al., 2024), especially when the distribution of thegauging stations is uneven.
500     Furthermore, the reliability of daily precipitation measurements in mountainous areas is compromised by issues such as gauge undercatch (Pritchard, 2021). Such challenges hinder our ability to thoroughly test MOS models across an entire region and thus to gain confidence in their use for operational post-processing of RCM daily precipitation.

    Another important limitation of the study relates to the lack of spatial coherence when sampling from the predicted probability distributions. The GPR post-processing approach, as implemented in this work, assumes that the daily precipitation
505     probability for each grid cell, conditional on a set of input features, is independent of its neighbours. This assumption, coupled with the large variability of precipitation in the region, leads to scattered precipitation occurrence maps when drawing independent samples from the predicted probability distribution at each location across the grid (Fig. 8d). This is therefore an area for potential improvement in future work by, for example, adding a latent variable that is defined across space (and/or any other dimensions, e.g., elevation) and builds correlations between neighbouring locations.
510     Disaggregating results spatially and temporally is important to assess the extent to which different MOS post-processing models improve results at finer scales. In this work, we have presented results (dis)aggregated at the regional level, enabling an

analysis of regional differences. However, further spatial granularity (e.g., at the station level) would potentially lead to a better understanding of model performance across different elevations and latitudes. Seasonality of precipitation also varies greatly across the three study regions. For example, the winter westerlies are responsible for much of the annual precipitation in West

515 UIB, whilst East UIB and Central UGB are summer monsoon dominated (Bookhagen and Burbank, 2010; Palazzi et al., 2013; Dimri et al., 2015). Given their relevance when it comes to impacts on water resources, flooding, and other rainfall-induced natural disasters, correctly post-processing dominating seasons for each region is another important aspect to assess. To some extent, optimising GPR models to perform best across all seasons inherently weights seasons by their relative significance. However, this work does not explicitly optimise models by season. This is therefore a direction that could be explored in future

520 work.

Although we considered various parametric distributions for modelling the conditional probability over daily precipitation and found that the Bernoulli gamma mixture model is a previously-used, robust, and effective choice (Williams, 1998; Cannon, 2008), we suggest further work be focused on the study of distributions for modelling the probability over daily precipitation (conditional on a set of variables). Finally, as we have shown that RCM post-processing patterns learned from one region

525 may be relevant for post-processing other (poorly gauged or completely ungauged) regions, future effort should be devoted to investigating the benefits of applying transfer learning (Pan and Yang, 2010) and meta-learning (Vanschoren, 2018) techniques for mountainous / data sparse regions like HKH, i.e., involving a model being pre-trained using data from a set of regions (especially those that are relatively data-rich, such as the Alps) and then fine-tuned for a different region or set of regions.

## 5 Conclusions

530 The compound effect of the local-scale variability and sparse observations that characterise daily precipitation in HKH poses a significant challenge when it comes to post-processing RCM outputs for ungauged locations. In this work, we address this issue by introducing a Generalised Probabilistic Regression (GPR) approach to MOS post-processing (i.e., downscaling and bias-correcting) of RCM-simulated daily precipitation hindcasts for ungauged mountain locations using sparse in situ observations. We test the GPR approach across three HKH regions and four experiments that mimic real-world scenarios. These experiments

535 explore the ability of GPR models to generalise to: 1) ungauged locations within each region using separate-region models, 2) ungauged locations within each region using combined-region models, 3) an entirely ungauged region using combined-region models, and 4) high-elevation ungauged locations within each region using separate-region models.

Overall, the three GPR model architectures we employ exhibit similar and consistently large performance improvements relative to both the WRF baseline and the $WRF_{SF}$ deterministic bias correction approach. Generalised linear models (VGLMs)

540 are found to be a robust choice for GPR-based post-processing of WRF daily precipitation but non-linear models ($MLP_S$ and $MLP_L$) do, in most cases, lead to improved performance. We find that GPR models are able to learn from sparsely distributed (both spatially and temporally) in situ observations and to generalise to new locations, using both separate-region or combined-region training settings. Performance of separate-region and combined-region GPR models is largely similar, resulting in much improved skill relative to WRF and $WRF_{SF}$. Combined-region GPR models are also capable of generalising to new (completely

545 ungauged) regions by leveraging data from other two regions. Although there is an expected drop in performance compared to other experiments, this experiment still results in large skill improvements relative to WRF and WRF$_{\text{SF}}$, with simpler model architectures being more robust choices in this setting. Furthermore, we explore the degree to which GPR models are effective at post-processing ungauged high-elevation locations and find that their performance is consistent with previous experiments, suggesting that this approach could be used to better understand much of the ungauged high-elevation regions of HKH.

550 GPR model performance exhibits large regional variability, driven by a combination of factors including the availability of in situ observations, performance/bias of WRF baseline and hydro-meteorological characteristics of each region. Simple GPR models are best for large precipitation events. The differential influence that input variables have for different GPR models underscores the complex interplay between input features and GPR model architecture, with thermodynamic/cloud related input variables being especially important. Lastly, our results show that GPR models can use patterns learned from one region to improve RCM post-processing in other region, and we therefore suggest/hypothesise that transfer learning and meta-learning may be promising approaches to leverage observations/knowledge from data-rich mountain regions (e.g., Alps) to improve RCM post-processing in other (data-poor) regions.

*Code and data availability.* The code used to reproduce the experiments, generate figures, and analyse the results presented in this study is available at: https://github.com/mgironamata/pddp-mountains. The WRF simulation output is available via Norris et al. (2019). The SRTM
560 elevation data is available at: https://earthexplorer.usgs.gov/. In situ gauge datasets were collected and provided by the Bhakra Beas Management Board and the Indian Meteorological Department (East UIB), the Pakistan Meteorological Department and the Water and Power Development Authority (West UIB), and the International Centre for Integrated Mountain Development (Central UGB). The authors of this paper do not have the required permission to make the gauge datasets publicly available but suggest that any readers interested in obtaining them contact the above organisations.

565 **Appendix A: Probability distributions**

**A1 Spike-and-slab mixture models**

To explicitly model the probability over both precipitation occurrence (zero and non-zero values) and magnitude we resort to a special type of mixture models called spike-and-slab models. A spike-and-slab model for a random variable $Y$ is a generative model in which $Y$ attains some fixed value $v$ (spike) or is drawn from a probability distribution $p$ (slab).

570 To implement a spike-and-slab model, let us consider a set of inputs $x_{1:M}$ and outputs $y_{1:M}$. Now, let $r_{1:M}$ be a collection of M additional binary values, the $m$-th of which is 1 if $y_m > 0$ and 0 if $y_m = 0$. Assume that observations $y_{1:M}$ are drawn from a collection of random variables $Y_{1:M}$, respectively. Assume that $r_{1:M}$ are sampled independently from a Bernoulli distribution. Following that, $y_m$ is zero if $r_m$ is zero, and sampled from a continuous distribution with support $(0, \infty)$ (e.g., gamma or log-normal) if $r_m$ is one. Below we detail the probabilistic models and associated conditional log-probability for various mixture
575 models of this type.

If we choose a gamma distribution with parameters $\alpha_m$ and $\beta_m$ to model the continuous part of the distribution, $y_m$ is produced via the following probabilistic model:

$$r_m \sim \mathcal{B}(\pi_m),$$
$$(y_m | r_m = 1) \sim \Gamma(\alpha_m, \beta_m)$$

We call this model a Bernoulli gamma mixture model, for which the conditional log-probability of the collection of $(y, r)_{1:M}$
580   value pairs is given by:

$$\sum_{m=1}^{M} \log p(y_m, r_m | x_m)$$
$$= \sum_{m=1}^{M} \log \mathcal{B}(r_m; \pi_m) \Gamma(y_m; \alpha_m, \beta_m)^{r_m}$$
$$= \sum_{m=1}^{M} r_m [\log \pi_m + \log \Gamma(y_m; \alpha_m, \beta_m)] + (1 - r_m) \log(1 - \pi_m)$$

# References

595    Andermann, C., Bonnet, S., and Gloaguen, R.: Evaluation of precipitation data sets along the Himalayan front, Geochemistry, Geophysics, Geosystems, 12, 1–16, https://doi.org/10.1029/2011GC003513, 2011.

Angus, M., Widmann, M., Orr, A., Ashrit, R., Leckebusch, G. C., and Mitra, A.: A comparison of two statistical postprocessing methods for heavy-precipitation forecasts over India during the summer monsoon, Quarterly Journal of the Royal Meteorological Society, 150, 1865–1883, https://doi.org/10.1002/qj.4677, 2024.

600    Archer, D. R. and Fowler, H. J.: Spatial and temporal variations in precipitation in the Upper Indus Basin, global teleconnections and hydrological implications, Hydrology and Earth System Sciences, 8, 47–61, 2004.

Arfan, M., Lund, J., Hassan, D., Saleem, M., and Ahmad, A.: Assessment of spatial and temporal flow variability of the Indus River, Resources, 8, 1–17, https://doi.org/10.3390/resources8020103, 2019.

Bannister, D., Orr, A., Jain, S. K., Holman, I. P., Momblanch, A., Phillips, T., Adeloye, A. J., Snapir, B., Waine, T. W., Hosk-
605    ing, J. S., and Allen-Sader, C.: Bias Correction of High-Resolution Regional Climate Model Precipitation Output Gives the Best Estimates of Precipitation in Himalayan Catchments, Journal of Geophysical Research: Atmospheres, 124, 14 220–14 239, https://doi.org/10.1029/2019JD030804, 2019.

Baño-Medina, J., Manzanas, R., and Gutierrez, J. M.: Configuration and intercomparison of deep learning neural models for statistical downscaling, Geoscientific Model Development, 13, 2109–2124, https://doi.org/10.5194/gmd-13-2109-2020, 2020.

610    Baudouin, J. P., Herzog, M., and Petrie, C. A.: Contribution of cross-barrier moisture transport to precipitation in the upper indus river basin, Monthly Weather Review, 148, 2801–2818, https://doi.org/10.1175/MWR-D-19-0384.1, 2020.

Beck, H. E., Wood, E. F., Pan, M., Fisher, C. K., Miralles, D. G., Van Dijk, A. I., McVicar, T. R., and Adler, R. F.: MSWEP V2 Global 3-hourly 0.1° Precipitation: Methodology and Quantitative Assessment, Bulletin of the American Meteorological Society, 100, 473–500, https://doi.org/10.1175/BAMS-D-17-0138.1, 2019.

615    Bhardwaj, A., Wasson, R. J., Chow, W. T., and Ziegler, A. D.: High-intensity monsoon rainfall variability and its attributes: a case study for Upper Ganges Catchment in the Indian Himalaya during 1901–2013, Natural Hazards, 105, 2907–2936, https://doi.org/10.1007/s11069-020-04431-9, 2021.

Bolch, T., Kulkarni, A. V., Kääb, A., Huggel, C., Paul, F., Cogley, J. G., Frey, H., Kargel, J. S., Fujita, K., Scheel, M., Bajracharya, S., and Stoffel, M.: The state and fate of Himalayan glaciers., Science, 336, 310–4, https://doi.org/10.1126/science.1215828, 2012.

620    Bookhagen, B. and Burbank, D. W.: Toward a complete Himalayan hydrological budget: Spatiotemporal distribution of snowmelt and rainfall and their impact on river discharge, Journal of Geophysical Research: Earth Surface, 115, 1–25, https://doi.org/10.1029/2009JF001426, 2010.

Burt, D. R., Shen, Y., and Broderick, T.: Consistent Validation for Predictive Methods in Spatial Settings, http://arxiv.org/abs/2402.03527, 2024.

625    Cannon, A. J.: Probabilistic multisite precipitation downscaling by an expanded Bernoulli-gamma density network, Journal of Hydrometeorology, 9, 1284–1300, https://doi.org/10.1175/2008JHM960.1, 2008.

Chinnasamy, P., Bharati, L., Bhattarai, U., Khadka, A., Dahal, V., and Wahid, S.: Impact of planned water resource development on current and future water demand in the Koshi River basin, Nepal, Water International, 40, 1004–1020, https://doi.org/10.1080/02508060.2015.1099192, 2015.

630  Das, S., Ashrit, R., and Moncrieff, M. W.: Simulation of a Himalayan cloudburst event, Journal of Earth System Science 2006 115:3, 115, 299–313, https://doi.org/10.1007/BF02702044, 2006.

De Wit, A. J. W., Boogaard, H. L., and Van Diepen, C. A.: Spatial resolution of precipitation and radiation: The effect on regional crop yield forecasts, Agricultural and Forest Meteorology, pp. 156–168, https://doi.org/10.1016/j.agrformet.2005.11.012, 2005.

Dimri, A. P.: Bias correction demonstration in two of the Indian Himalayan river basins, Journal of Water and Climate Change, 12, 1297–
635  1309, https://doi.org/10.2166/wcc.2020.119, 2021.

Dimri, A. P., Niyogi, D., Barros, A. P., Ridley, J., Mohanty, U. C., Yasunari, T., and Sikka, D. R.: Western Disturbances: A review, Reviews of Geophysics, 53, 225–246, https://doi.org/10.1002/2014RG000460, 2015.

Dimri, A. P., Chevuturi, A., Niyogi, D., Thayyen, R. J., Ray, K., Tripathi, S. N., Pandey, A. K., and Mohanty, U. C.: Cloudbursts in Indian Himalayas: A review, Earth-Science Reviews, 168, 1–23, https://doi.org/10.1016/j.earscirev.2017.03.006, 2017.

640  Eden, J. M., Widmann, M., Grawe, D., and Rast, S.: Skill, correction, and downscaling of GCM-simulated precipitation, Journal of Climate, 25, 3970–3984, https://doi.org/10.1175/JCLI-D-11-00254.1, 2012.

Giorgi, F.: Thirty Years of Regional Climate Modeling: Where Are We and Where Are We Going next?, Journal of Geophysical Research: Atmospheres, 124, 5696–5723, https://doi.org/10.1029/2018JD030094, 2019.

Gneiting, T. and Raftery, A. E.: Strictly proper scoring rules, prediction, and estimation, Journal of the American Statistical Association, 102,
645  359–378, https://doi.org/10.1198/016214506000001437, 2007.

Hersbach, H., Bell, B., Berrisford, P., Hirahara, S., Horányi, A., Muñoz-Sabater, J., Nicolas, J., Peubey, C., Radu, R., Schepers, D., Simmons, A., Soci, C., Abdalla, S., Abellan, X., Balsamo, G., Bechtold, P., Biavati, G., Bidlot, J., Bonavita, M., De Chiara, G., Dahlgren, P., Dee, D., Diamantakis, M., Dragani, R., Flemming, J., Forbes, R., Fuentes, M., Geer, A., Haimberger, L., Healy, S., Hogan, R. J., Hólm, E., Janisková, M., Keeley, S., Laloyaux, P., Lopez, P., Lupu, C., Radnoti, G., de Rosnay, P., Rozum, I., Vamborg, F., Vil-
650  laume, S., and Thépaut, J. N.: The ERA5 global reanalysis, Quarterly Journal of the Royal Meteorological Society, 146, 1999–2049, https://doi.org/10.1002/qj.3803, 2020.

Huang, Y., Bárdossy, A., and Zhang, K.: Sensitivity of hydrological models to temporal and spatial resolutions of rainfall data, Hydrology and Earth System Sciences, 23, 2647–2663, https://doi.org/10.5194/hess-23-2647-2019, 2019.

Huffman, G. J., Adler, R. F., Bolvin, D. T., Gu, G., Nelkin, E. J., Bowman, K. P., Hong, Y., Stocker, E. F., and Wolff, D. B.: The TRMM
655  Multisatellite Precipitation Analysis (TMPA): Quasi-Global, Multiyear, Combined-Sensor Precipitation Estimates at Fine Scales, Journal of Hydrometeorology, 8, 38–55, https://doi.org/10.1175/JHM560.1, 2007.

Immerzeel, W. W., van Beek, L. P. H., and Bierkens, M. F. P.: Climate change will affect the Asian water towers., Science (New York, N.Y.), 328, 1382–1385, https://doi.org/10.1126/science.1183188, 2010.

Immerzeel, W. W., Petersen, L., Ragettli, S., and Pellicciotti, F.: The importance of observed gradients of air temperature and pre-
660  cipitation for modeling runoff from a glacierized watershed in the Nepalese Himalayas, Water Resources Research, 50, 2212–2226, https://doi.org/10.1002/2013WR014506, 2014.

Immerzeel, W. W., Wanders, N., Lutz, A. F., Shea, J. M., and Bierkens, M. F.: Reconciling high-altitude precipitation in the upper Indus basin with glacier mass balances and runoff, Hydrology and Earth System Sciences, 19, 4673–4687, https://doi.org/10.5194/hess-19-4673-2015, 2015.

665  Iqbal, Z., Shahid, S., Ahmed, K., Ismail, T., and Nawaz, N.: Spatial distribution of the trends in precipitation and precipitation extremes in the sub-Himalayan region of Pakistan, Theoretical and Applied Climatology, 137, 2755–2769, https://doi.org/10.1007/s00704-019-02773-4, 2019.

Ji, X., Li, Y., Luo, X., He, D., Guo, R., Wang, J., Bai, Y., Yue, C., and Liu, C.: Evaluation of bias correction methods for APHRODITE data to improve hydrologic simulation in a large Himalayan basin, Atmospheric Research, 242, 104 964, https://doi.org/10.1016/j.atmosres.2020.104964, 2020.

Kingma, D. P. and Ba, J. L.: Adam: A method for stochastic optimization, in: 3rd International Conference on Learning Representations, ICLR 2015 - Conference Track Proceedings, 2015.

Klein, W. H. and Glahn, H. R.: Forecasting Local Weather by Means of Model Output Statistics, Bulletin of the American Meteorological Society, 55, 1217–1227, https://doi.org/10.1175/1520-0477(1974)055<1217:flwbmo>2.0.co;2, 1974.

Kokhlikyan, N., Miglani, V., Martin, M., Wang, E., Alsallakh, B., Reynolds, J., Melnikov, A., Kliushkina, N., Araya, C., Yan, S., and Reblitz-Richardson, O.: Captum: A unified and generic model interpretability library for PyTorch, Tech. rep., 2020.

Krishnan, R., Shrestha, A. B., Ren, G., Rajbhandari, R., Saeed, S., Sanjay, J., Syed, M. A., Vellore, R., Xu, Y., You, Q., and Ren, Y.: Unravelling Climate Change in the Hindu Kush Himalaya: Rapid Warming in the Mountains and Increasing Extremes, pp. 57–97, Springer International Publishing, Cham, ISBN 978-3-319-92288-1, https://doi.org/10.1007/978-3-319-92288-1_3, 2019.

Lafon, T., Dadson, S., Buys, G., and Prudhomme, C.: Bias correction of daily precipitation simulated by a regional climate model: a comparison of methods, International Journal of Climatology, 33, 1367–1381, https://doi.org/10.1002/joc.3518, 2013.

Li, H., Haugen, J. E., and Xu, C. Y.: Precipitation pattern in the Western Himalayas revealed by four datasets, Hydrology and Earth System Sciences, 22, 5097–5110, https://doi.org/10.5194/hess-22-5097-2018, 2018.

Li, L., Gochis, D. J., Sobolowski, S., and Mesquita, M. D.: Evaluating the present annual water budget of a Himalayan headwater river basin using a high-resolution atmosphere-hydrology model, Journal of Geophysical Research, 122, 4786–4807, https://doi.org/10.1002/2016JD026279, 2017.

Li, Z., Brissette, F., and Chen, J.: Finding the most appropriate precipitation probability distribution for stochastic weather generation and hydrological modelling in Nordic watersheds, Hydrological Processes, 27, 3718–3729, https://doi.org/10.1002/hyp.9499, 2013.

Luo, X., Fan, X., Ji, X., and Li, Y.: Evaluation of corrected APHRODITE estimates for hydrological simulation in the Yarlung Tsangpo–Brahmaputra River Basin, International Journal of Climatology, 40, 4158–4170, https://doi.org/10.1002/JOC.6449, 2020.

Lutz, A. F., Immerzeel, W. W., Kraaijenbrink, P. D., Shrestha, A. B., and Bierkens, M. F.: Climate change impacts on the upper indus hydrology: Sources, shifts and extremes, PLoS ONE, 11, e0165 630, https://doi.org/10.1371/journal.pone.0165630, 2016.

Maraun, D.: Bias correction, quantile mapping, and downscaling: Revisiting the inflation issue, Journal of Climate, 26, 2137–2143, https://doi.org/10.1175/JCLI-D-12-00821.1, 2013.

Maraun, D. and Widmann, M.: Statistical Downscaling and Bias Correction for Climate Research, Cambridge University Press, ISBN 9788578110796, 2018.

Maussion, F., Scherer, D., Finkelnburg, R., Richters, J., Yang, W., and Yao, T.: WRF simulation of a precipitation event over the Tibetan Plateau, China - An assessment using remote sensing and ground observations, Hydrology and Earth System Sciences, 15, 1795–1817, https://doi.org/10.5194/HESS-15-1795-2011, 2011.

Medina, S., Houze, R. A., Kumar, A., and Niyogi, D.: Summer monsoon convection in the Himalayan region: Terrain and land cover effects, Quarterly Journal of the Royal Meteorological Society, 136, 593–616, https://doi.org/10.1002/qj.601, 2010.

Momblanch, A., Papadimitriou, L., Jain, S. K., Kulkarni, A., Ojha, C. S., Adeloye, A. J., and Holman, I. P.: Untangling the water-food-energy-environment nexus for global change adaptation in a complex Himalayan water resource system, Science of the Total Environment, 655, 35–47, https://doi.org/10.1016/j.scitotenv.2018.11.045, 2019.

705  Mukherji, A., Sinisalo, A., Nüsser, M., Garrard, R., and Eriksson, M.: Contributions of the cryosphere to mountain communities in the Hindu Kush Himalaya: A review, Regional Environmental Change, 19, 1311–1326, https://doi.org/10.1007/s10113-019-01484-w, 2019.

Nepal, S., Steiner, J. F., Allen, S., Azam, M. F., Bhuchar, S., Biemans, H., Dhakal, M., Khanal, S., Li, D., Lutz, A., Pradhananga, S., Ritzema, R., Stoffel, M., and Stuart-Smith, R.: Consequences of cryospheric change for water resources and hazards in the Hindu Kush Himalaya Consequences of cryospheric change for water resources and hazards in the Hindu Kush Himalaya. In ICIMOD (P. Wester, S. Chaudhary,

710  N. Chettri, M. Jackson, A. Mah, in: Water, ice, society, and ecosystems in the Hindu Kush Himalaya: An outlook, pp. 73–121, ICIMOD, https://doi.org/https://doi. org/10.53055/ICIMOD.1031, 2023.

Nie, Y., Pritchard, H. D., Liu, Q., Hennig, T., Wang, W., Wang, X., Liu, S., Nepal, S., Samyn, D., Hewitt, K., and Chen, X.: Glacial change and hydrological implications in the Himalaya and Karakoram, Nature Reviews Earth and Environment, 2, 91–106, https://doi.org/10.1038/s43017-020-00124-w, 2021.

715  Norris, J., Carvalho, L. M., Jones, C., Cannon, F., Bookhagen, B., Palazzi, E., and Tahir, A. A.: The spatiotemporal variability of precipitation over the Himalaya: evaluation of one-year WRF model simulation, Climate Dynamics, 49, 2179–2204, https://doi.org/10.1007/s00382-016-3414-y, 2017.

Norris, J., Carvalho, L. M., Jones, C., and Cannon, F.: Deciphering the contrasting climatic trends between the central Himalaya and Karakoram with 36 years of WRF simulations, Climate Dynamics, 52, 159–180, https://doi.org/10.1007/s00382-018-4133-3, 2019.

720  Norris, J., Carvalho, L. M., Jones, C., and Cannon, F.: Warming and drying over the central Himalaya caused by an amplification of local mountain circulation, npj Climate and Atmospheric Science, 3, 1–11, https://doi.org/10.1038/s41612-019-0105-5, 2020.

Orr, A., Listowski, C., Couttet, M., Collier, E., Immerzeel, W. W., Deb, P., and Bannister, D.: Sensitivity of simulated summer monsoonal precipitation in Langtang Valley, Himalaya, to cloud microphysics schemes in WRF, Journal of Geophysical Research, 122, 6298–6318, https://doi.org/10.1002/2016JD025801, 2017.

725  Orr, A., Ahmad, B., Alam, U., Appadurai, A. N., Bharucha, Z. P., Biemans, H., Bolch, T., Chaulagain, N. P., Dhaubanjar, S., Dimri, A. P., Dixon, H., Fowler, H. J., Gioli, G., Halvorson, S. J., Hussain, A., Jeelani, G., Kamal, S., Khalid, I. S., Liu, S., Lutz, A., Mehra, M. K., Miles, E., Momblanch, A., Muccione, V., Mukherji, A., Mustafa, D., Najmuddin, O., Nasimi, M. N., Nüsser, M., Pandey, V. P., Parveen, S., Pellicciotti, F., Pollino, C., Potter, E., Qazizada, M. R., Ray, S., Romshoo, S., Sarkar, S. K., Sawas, A., Sen, S., Shah, A., Shah, M. A. A., Shea, J. M., Sheikh, A. T., Shrestha, A. B., Tayal, S., Tigala, S., Virk, Z. T., Wester, P., and Wescoat, J. L.: Knowledge Priorities on

730  Climate Change and Water in the Upper Indus Basin: A Horizon Scanning Exercise to Identify the Top 100 Research Questions in Social and Natural Sciences, Earth's Future, 10, e2021EF002 619, https://doi.org/10.1029/2021EF002619, 2022.

Palazzi, E., Von Hardenberg, J., and Provenzale, A.: Precipitation in the Hindu-Kush Karakoram Himalaya: Observations and future scenarios, Journal of Geophysical Research Atmospheres, 118, 85–100, https://doi.org/10.1029/2012JD018697, 2013.

Pan, S. J. and Yang, Q.: A survey on transfer learning, IEEE Transactions on Knowledge and Data Engineering, 22, 1345–1359,
735  https://doi.org/10.1109/TKDE.2009.191, 2010.

Peleg, N., Fatichi, S., Athanasios, P., Molnar, P., and Burlando, P.: An advanced stochastic weather generator for simulating 2-D high-resolution climate variables, Journal of Advances in Modeling Earth Systems, pp. 1595–1627, https://doi.org/10.1002/2016MS000854, 2017.

Potter, E. R., Orr, A., Willis, I. C., Bannister, D., and Salerno, F.: Dynamical Drivers of the Local Wind Regime in a Himalayan Valley,
740  Journal of Geophysical Research: Atmospheres, 123, 13,186–13,202, https://doi.org/10.1029/2018JD029427, 2018.

Pritchard, H. D.: Global Data Gaps in Our Knowledge of the Terrestrial Cryosphere, Frontiers in Climate, 3, 1–7, https://doi.org/10.3389/fclim.2021.689823, 2021.

Qazi, N. Q., Jain, S. K., Thayyen, R. J., Patil, P. R., and Singh, M. K.: Hydrology of the himalayas, in: Himalayan Weather and Climate and their Impact on the Environment, pp. 419–450, Springer International Publishing, ISBN 9783030296841, https://doi.org/10.1007/978-3-030-29684-1_21, 2019.

745 Ramezani Ziarani, M., Bookhagen, B., Schmidt, T., Wickert, J., de la Torre, A., and Hierro, R.: Using convective available potential energy (CAPE) and dew-point temperature to characterize rainfall-extreme events in the SOUTHCENTRAL ANDES, Atmosphere, 10, 1–22, https://doi.org/10.3390/atmos10070379, 2019.

Ren, Y. Y., Ren, G. Y., Sun, X. B., Shrestha, A. B., You, Q. L., Zhan, Y. J., Rajbhandari, R., Zhang, P. F., and Wen, K. M.: Observed changes

750 in surface air temperature and precipitation in the Hindu Kush Himalayan region over the last 100-plus years, Advances in Climate Change Research, 8, 148–156, https://doi.org/10.1016/j.accre.2017.08.001, 2017.

Rumelhart, D. E., Hinton, G. E., and Williams, R. J.: Learning representations by back-propagating errors, Nature, 323, 533–536, https://doi.org/10.1038/323533a0, 1986.

Sabin, T. P., Krishnan, R., Vellore, R., Priya, P., Borgaonkar, H. P., Singh, B. B., and Sagar, A.: Climate Change Over the Himalayas, in:

755 Assessment of Climate Change over the Indian Region: A Report of the Ministry of Earth Sciences (MoES), Government of India, pp. 207–222, Springer Singapore, ISBN 9789811543272, https://doi.org/10.1007/978-981-15-4327-2_11, 2020.

Sachindra, D. A., Ahmed, K., Rashid, M. M., Shahid, S., and Perera, B. J.: Statistical downscaling of precipitation using machine learning techniques, Atmospheric Research, 212, 240–258, https://doi.org/10.1016/j.atmosres.2018.05.022, 2018.

Saha, S., Moorthi, S., Pan, H. L., Wu, X., Wang, J., Nadiga, S., Tripp, P., Kistler, R., Woollen, J., Behringer, D., Liu, H., Stokes, D., Grumbine,

760 R., Gayno, G., Wang, J., Hou, Y. T., Chuang, H. Y., Juang, H. M. H., Sela, J., Iredell, M., Treadon, R., Kleist, D., Van Delst, P., Keyser, D., Derber, J., Ek, M., Meng, J., Wei, H., Yang, R., Lord, S., Van Den Dool, H., Kumar, A., Wang, W., Long, C., Chelliah, M., Xue, Y., Huang, B., Schemm, J. K., Ebisuzaki, W., Lin, R., Xie, P., Chen, M., Zhou, S., Higgins, W., Zou, C. Z., Liu, Q., Chen, Y., Han, Y., Cucurull, L., Reynolds, R. W., Rutledge, G., and Goldberg, M.: The NCEP Climate Forecast System Reanalysis, Bulletin of the American Meteorological Society, 91, 1015–1058, https://doi.org/10.1175/2010BAMS3001.1, 2010.

765 Salzmann, N., Huggel, C., Rohrer, M., and Stoffel, M.: Data and knowledge gaps in glacier, snow and related runoff research - A climate change adaptation perspective, Journal of Hydrology, 518, 225–234, https://doi.org/10.1016/j.jhydrol.2014.05.058, 2014.

Samuel, J., Coulibaly, P., and Metcalfe, R. A.: Evaluation of future flow variability in ungauged basins: Validation of combined methods, Advances in Water Resources, 35, 121–140, https://doi.org/10.1016/j.advwatres.2011.09.015, 2012.

Sanjay, J., Krishnan, R., Shrestha, A. B., Rajbhandari, R., and Ren, G. Y.: Downscaled climate change projections for the Hindu

770 Kush Himalayan region using CORDEX South Asia regional climate models, Advances in Climate Change Research, 8, 185–198, https://doi.org/10.1016/j.accre.2017.08.003, 2017.

Shea, J. M., Wagnon, P., Immerzeel, W. W., Biron, R., Brun, F., and Pellicciotti, F.: A comparative high-altitude meteorological analysis from three catchments in the Nepalese Himalaya, International Journal of Water Resources Development, 31, 174–200, https://doi.org/10.1080/07900627.2015.1020417, 2015.

775 Shrestha, F., Steiner, J. F., Shrestha, R., Dhungel, Y., Joshi, S. P., Inglis, S., Ashraf, A., Wali, S., Walizada, K. M., and Zhang, T.: A comprehensive and version-controlled database of glacial lake outburst floods in High Mountain Asia, Earth System Science Data, 15, 3941–3961, https://doi.org/10.5194/essd-15-3941-2023, 2023.

Shrestha, M., Acharya, S. C., and Shrestha, P. K.: Bias correction of climate models for hydrological modelling - are simple methods still useful?, Meteorological Applications, 24, 531–539, https://doi.org/10.1002/met.1655, 2017.

780    Song, P. X.-K.: Vector Generalized Linear Models, pp. 121–155, Springer New York, New York, NY, ISBN 978-0-387-71393-9, https://doi.org/10.1007/978-0-387-71393-9_6, 2007.

Steiner, J. F., Gurung, T. R., Joshi, S. P., Koch, I., Saloranta, T., Shea, J., Shrestha, A. B., Stigter, E., and Immerzeel, W. W.: Multi-year observations of the high mountain water cycle in the Langtang catchment, Central Himalaya, Hydrological Processes, 35, 1–7, https://doi.org/10.1002/hyp.14189, 2021.

785    Tazi, K., Orr, A., Hernandez-González, J., Hosking, S., and Turner, R. E.: High Mountain Asia using Multi-Fidelity Gaussian Processes: Improved estimates from ERA5, EGUsphere [preprint], https://doi.org/https://doi.org/10.5194/egusphere-2023-2145, 2023.

Thayyen, R. J., Dimri, A. P., Kumar, P., and Agnihotri, G.: Study of cloudburst and flash floods around Leh, India, during August 4-6, 2010, Natural Hazards, 65, 2175–2204, https://doi.org/10.1007/s11069-012-0464-2, 2013.

Thornton, J. M., Pepin, N., Shahgedanova, M., and Adler, C.: Coverage of In Situ Climatological Observations in the World's Mountains,
790    Frontiers in Climate, 4, 1–20, https://doi.org/10.3389/fclim.2022.814181, 2022.

ul Hasson, S., Böhner, J., and Chishtie, F.: Low fidelity of CORDEX and their driving experiments indicates future climatic uncertainty over Himalayan watersheds of Indus basin, Climate Dynamics, 52, 777–798, https://doi.org/10.1007/S00382-018-4160-0/FIGURES/16, 2019.

Vandal, T., Kodra, E., and Ganguly, A. R.: Intercomparison of machine learning methods for statistical downscaling: the case of daily and extreme precipitation, Theoretical and Applied Climatology, 137, 557–570, https://doi.org/10.1007/s00704-018-2613-3, 2019.

795    Vanschoren, J.: Meta-Learning: A Survey, pp. 1–29, http://arxiv.org/abs/1810.03548, 2018.

Vaughan, A., Tebbutt, W., Hosking, J. S., and Turner, R. E.: Convolutional conditional neural processes for local climate downscaling, Tech. rep., 2021.

Wang, X., Tolksdorf, V., Otto, M., and Scherer, D.: WRF-based dynamical downscaling of ERA5 reanalysis data for High Mountain Asia: Towards a new version of the High Asia Refined analysis, International Journal of Climatology, 41, 743–762,
800    https://doi.org/10.1002/joc.6686, 2021.

Wester, P., Mishra, A., Mukherji, A., and Shrestha, A. B.: The Hindu Kush Himalaya Assessment - Mountains, Climate Change, Sustainability and People, Springer Nature Switzerland AG, Cham, ISBN 9783319922874, https://doi.org/10.1007/978-3-319-92288-1_8, 2019.

Widmann, M., Blake, R., Sooraj, K., Orr, A., Sanjay, J., Karumuri, A., Mitra, A., Rajagopal, E., Van Loon, A. F., Hannah, D., Barrand, N., Singh, R., Mishra, V., Sudgen, F., and Arya, D.: Current Opportunities and Challenges in Developing Hydro-Climatic Services in
805    the Himalayas Report of Pump Priming Project 2017. Centre for Ecology & Hydrology, Wallingford and Indian Institute of Tropical Meteorology, Pune, Tech. rep., https://nora.nerc.ac.uk/id/eprint/528847/, 2019.

Wilks, D. S.: Statistical Methods in the Atmospheric Sciences, vol. 91, Elsevier Inc., second edi edn., 2006.

Williams, P. M.: Modelling seasonality and trends in daily rainfall data, Advances in Neural Information Processing Systems, pp. 985–991, 1998.

810    Wong, G., Maraun, D., Vrac, M., Widmann, M., Eden, J. M., and Kent, T.: Stochastic Model Output Statistics for Bias Correcting and Downscaling Precipitation Including Extremes, Journal of Climate, 27, 6940–6959, https://doi.org/10.1175/JCLI-D-13-00604.1, 2014.

Wulf, H., Bookhagen, B., and Scherler, D.: Differentiating between rain, snow, and glacier contributions to river discharge in the western Himalaya using remote-sensing data and distributed hydrological modeling, Advances in Water Resources, 88, 152–169, https://doi.org/10.1016/j.advwatres.2015.12.004, 2016.

815    Xu, J., Badola, R., Chettri, N., Chaudhary, R. P., Zomer, R., Pokhrel, B., Hussain, S. A., Pradhan, S., and Pradhan, R.: Sustaining Biodiversity and Ecosystem Services in the Hindu Kush Himalaya, pp. 127–165, Springer International Publishing, Cham, ISBN 978-3-319-92288-1, https://doi.org/10.1007/978-3-319-92288-1_5, 2019.

Yatagai, A., Kamiguchi, K., Arakawa, O., Hamada, A., Yasutomi, N., and Kitoh, A.: APHRODITE: Constructing a Long-Term Daily Gridded
Precipitation Dataset for Asia Based on a Dense Network of Rain Gauges, Bulletin of the American Meteorological Society, 93, 1401–

820   1415, https://doi.org/10.1175/BAMS-D-11-00122.1, 2012.

Zeiler, M. D. and Fergus, R.: Visualizing and Understanding Convolutional Networks, in: Computer Vision – ECCV 2014, edited by Fleet
David, Pajdla, T., Bernt, S., and Tinne, T., pp. 818–833, Springer International Publishing, Cham, ISBN 978-3-319-10590-1, 2014.